



---

Simple Multiresolution Filtering and the Spectra of Radio Galaxies and Supernova Remnants

Author(s): L. Rudnick

Source: *Publications of the Astronomical Society of the Pacific*, Vol. 114, No. 794 (April 2002), pp. 427-449

Published by: Astronomical Society of the Pacific

Stable URL: <https://www.jstor.org/stable/10.1086/342499>

Accessed: 16-04-2022 20:33 UTC

---

JSTOR is a not-for-profit service that helps scholars, researchers, and students discover, use, and build upon a wide range of content in a trusted digital archive. We use information technology and tools to increase productivity and facilitate new forms of scholarship. For more information about JSTOR, please contact [support@jstor.org](mailto:support@jstor.org).

Your use of the JSTOR archive indicates your acceptance of the Terms & Conditions of Use, available at <https://about.jstor.org/terms>



JSTOR

*Astronomical Society of the Pacific* is collaborating with JSTOR to digitize, preserve and extend access to *Publications of the Astronomical Society of the Pacific*

# Simple Multiresolution Filtering and the Spectra of Radio Galaxies and Supernova Remnants

L. RUDNICK

Astronomy Department, University of Minnesota, 116 Church Street SE, Minneapolis, MN 55455

Received 2001 August 14; accepted 2002 January 23

**ABSTRACT.** A simple method is explored for examining the structures and spectral index distributions on different scales in Galactic and extragalactic radio sources, based on a multiresolution filtering technique suggested by Starck, Murtagh, & Bijaoui. Multiresolution filtering, whether in this simple algorithm or more sophisticated ones, is also useful for a wide variety of image analysis purposes. For spectral index studies, the filtering is complementary to other methods and is especially useful in separating large-scale and small-scale features with different spectral distributions. In this paper, filtered spectral distributions are produced for several sources. In the extragalactic sources, different spectral gradients are found for narrow and broad features as a function of distance from the terminal hot spots. This complicates the standard analyses used to understand relativistic particle acceleration and losses. We show that the high-field regions can yield either flatter or steeper spectra than low-field regions and be either brighter or fainter, depending on the particle history. In our supernova remnant example, Cas A, the spectra of the fine-scale features are found, in the mean, to be flatter than those on larger scales. In addition, a clear asymmetry is found in the spectral indices of the largest scale emission and is related to other physical properties of the remnant.

## 1. INTRODUCTION

The broadband spectra of Galactic and extragalactic radio sources provide information on the relativistic electron populations and their evolution. The standard techniques used to derive the “spectral index maps,” however, are subject to a number of problems. As shown by Katz-Stone, Rudnick, & Anderson (1993), there is often substantial confusion from overlapping structures along the line of sight in radio galaxies. This can lead to inappropriate physical models for the sources, their energetics, ages, etc. In supernova remnants (SNRs), the spectral variations are often small, and a two-frequency regression analysis (“T-T”) must often be done over a large area to avoid biases from low-level backgrounds (Leahy & Roger 1991). Since the sites and scale sizes for particle acceleration are currently not understood, this presents a major limitation for SNR studies.

In this paper, we explore the use of an extremely simple multiresolution filtering technique, based on a description of these algorithms in Starck, Murtagh, & Bijaoui (1998, § 1.6). The decomposition of images into structures on different scales is a long-standing problem, e.g., for pattern-recognition algorithms, and Mallat (1989) introduced the use of an orthonormal wavelet basis for this purpose. Since then, wavelet decomposition has proved of substantial value in astronomical image processing (e.g., Sanz et al. 1999). The technique we explore here is a trivial multiresolution algorithm, based on anisotropic “top-hat” filters instead of orthonormal wavelets. Its primary

advantages are its simplicity, speed, and ability to reconstruct, with a reasonable degree of accuracy, continuous images with Gaussian noise, such as encountered in radio astronomy (e.g., Ledden et al. 1980). The technique has not been explored in the Poisson statistics limit.

We begin with a description of the existing methods of spectral index (equivalent to optical “color”) determination, followed by an introduction to the simple top-hat multiresolution filtering. We then use this to analyze both simulated and actual sources and discuss some of the interesting science that is immediately apparent from these decompositions. Readers primarily interested in the astrophysical implications for radio galaxies or SNRs should proceed to § 3 or § 4, respectively.

### 1.1. Summary of Spectral Index Determination Methods

*Direct division.*—This is the simplest and most direct method of determining the spectral index between maps  $S_1(x, y)$  and  $S_2(x, y)$  at two frequencies  $\nu_1$  and  $\nu_2$  and consists of calculating

$$\alpha_{1,2}(x, y) \equiv \frac{\log(S_1/S_2)}{\log(\nu_1/\nu_2)}.$$

This method, although the most direct, is subject to serious biases if there is a zero-level offset or large-scale gradients in one or both of the input maps. In radio astronomy, such offsets can arise from inadequate baselines in filled-aperture maps or missing short spacings on aperture-synthesis maps. The direct

division method also cannot isolate the spectral indices of features that are blended or superposed on the maps, such as the spectral index of a jet seen at low contrast against a background lobe. This is a major challenge in extragalactic source analysis.

*Regression.*—This method, used in SNR spectral analyses, where it is called the “T-T” method (e.g., Leahy & Roger 1991, 1998; Anderson & Rudnick 1996), is useful in the case where there is a constant or slowly varying background offset and structure on smaller scales. It involves least-squares fitting a parameter  $\alpha$ , such that

$$\chi_{\text{box}}^2(\alpha) = \sum_{\text{box}} \left[ S_2(x, y) - \left( \frac{\nu_2}{\nu_1} \right)^{\alpha(\text{box})} S_1(x, y) \right]^2$$

is minimized over different boxes on the map. Its advantage is that it makes use of all the small-scale variations in each box to remove the effects of any bias that is constant over the size of the box; its disadvantage is that it averages over the spectra of all the small-scale variations in the box and is confused by gradients in the diffuse emission.

*Modeling.*—If the shapes of the features under study can be adequately represented, e.g., as one- or two-dimensional Gaussians, then these can be fitted to the data at each frequency and the corresponding flux densities used to calculate spectra. This approach, as in the regression method discussed above, makes use of data from a region of finite size on the map and can thus yield an improvement in signal-to-noise ratio over direct division. However, multiple Gaussian fits are often not robust (see, e.g., Heiles & Troland 2002), and biases will also result when actual component shapes differ from the assumed shapes.

*Spectral tomography.*—This method is effective in one situation where all other methods fail, specifically, in separating overlapping features with different spectral indices even when they are on similar spatial scales. It involves forming a gallery of images,  $S_\alpha(x, y)$  as a function of  $\alpha$ , where

$$S_\alpha(x, y) = S_2(x, y) - \left( \frac{\nu_2}{\nu_1} \right)^\alpha S_1(x, y).$$

When  $\alpha$  is the same as the spectral index  $\alpha_0$  of some feature on the maps, that feature disappears from  $S_\alpha(x, y)$ . It is the disappearance of the feature that is used to determine its spectral index, and it can be seen even when the feature partially overlaps with another feature on the map. This technique has been used by Katz-Stone & Rudnick (1997), Hardcastle (1999), and Crawford et al. (2001) to discover and determine spectra for previously blended features.

The primary advantage to spectral tomography is that a coherent feature of arbitrary shape can be recognized and measured. The primary disadvantage is that it currently relies on a subjective decision on what constitutes a “feature” so that its disappearance and spectral index can be measured. This same subjectivity is present, but not made explicit, in the apparently

objective methods of modeling and regression as described above.

*Filtering.*—This class of analysis techniques involves removing emission from maps at both frequencies, often on large scales, and then performing a direct division, in order to measure the spectra of smaller scale features. It was used, e.g., by Wright et al. (1999) in their multifrequency analysis of Cas A by applying a bandpass filter in the Fourier plane. In terms of removing large-scale features, this is equivalent to subtracting a convolved image from the original one. Because it produces shallow extended negative bowls around small-scale features, this convolution method works well only where weaker features are sufficiently far from stronger ones.

## 2. MULTIREOLUTION FILTERING

We sought a simple algorithm for separating features of different scale sizes that would (1) allow the spectra of both large- and small-scale features to be measured, (2) avoid the negative bowls of convolution techniques, and (3) require little, if any, subjective judgment. A slightly modified version of the multi-scale morphological transform described by Starck et al. (1998, § 1.6) was found useful for this purpose. It depends on the construction of two maps—a “filtered” map and an “open” map as defined below—containing the small- and large-scale structure, respectively, from an original map. Lea & Kellar (1989) used a similar technique, based on the work of Serra (1982) for isolating objects from a varying background.

The open map and the filtered map at each frequency can then be respectively divided by their counterparts at a second frequency to calculate the spectral index distributions on large and small scales. In the following subsections, we discuss how different features are partitioned into the filtered and open maps and the fidelity of the partitioning and hence spectral index determination in both the presence and absence of noise.

### 2.1. Filtered Map Construction

Although we describe the construction in detail, its implementation is quite straightforward. Using the AIPS package, e.g., it requires only a three-line modification to the task “MWFLT” and a short external “procedure.”

We start with some definitions, based on the nomenclature from Starck et al. (1998). The term  $e_N[S_i(x, y)]$  is the *eroded* counterpart of  $S_i(x, y)$  with box size  $N$ . It is constructed by replacing each pixel on the image with the *minimum* of itself and the surrounding pixels in a box of size  $N \times N$ , where  $N$  is usually odd so that there is a center pixel. The term  $d_N[S_i(x, y)]$  is the *dilated* counterpart of  $S_i(x, y)$ , constructed by replacing each pixel on the image with the *maximum* of itself and the surrounding pixels in a box of size  $N$ . The process of performing first an erosion and then a dilation on a map

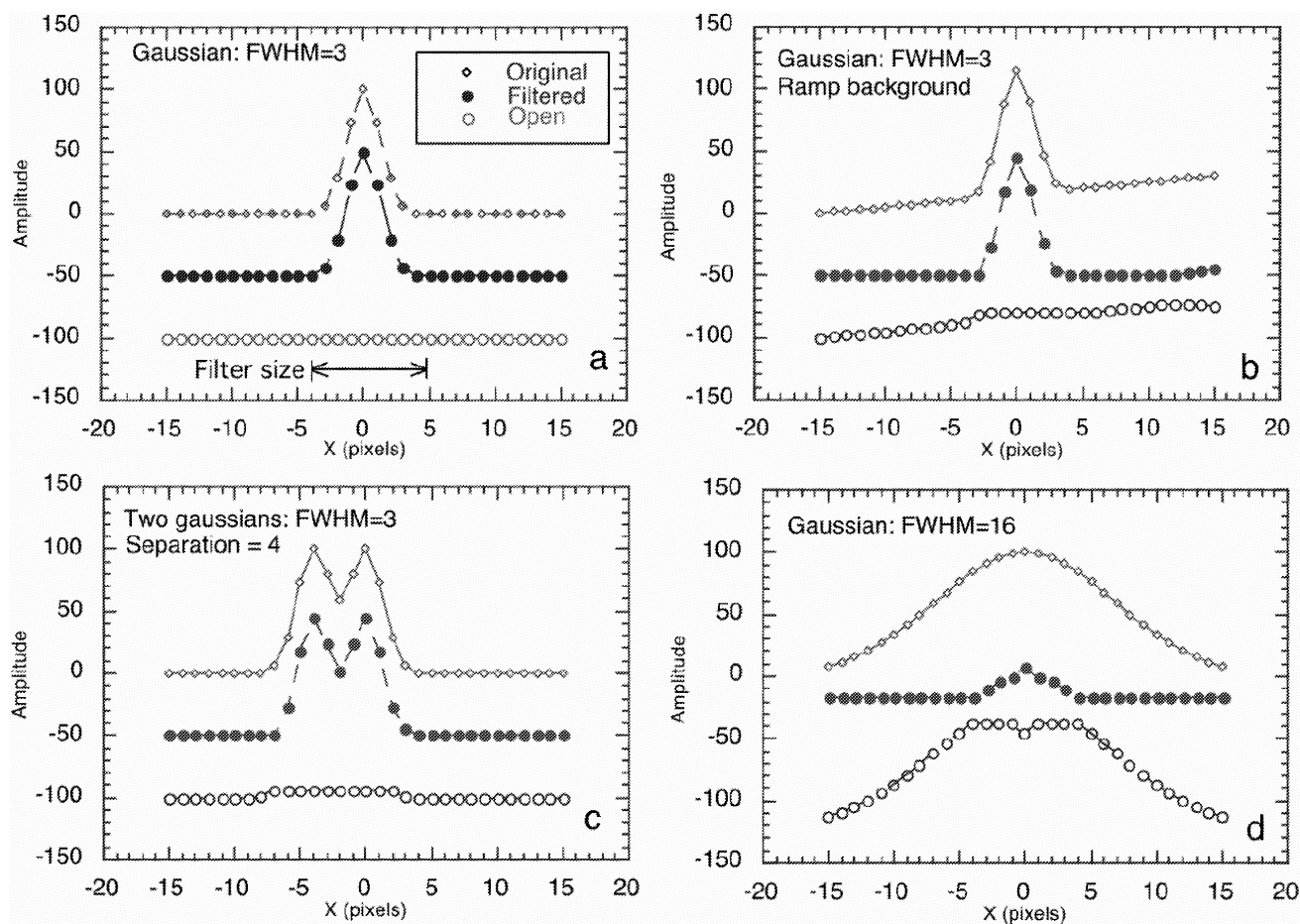


FIG. 1.—One-dimensional slices through Gaussian models showing partitioning of model map into opened and filtered components.

yields the map we define as *open*,  $o_N[S_i(x, y)]$ , i.e.,

$$o_N[S_i(x, y)] \equiv d_N\{e_N[S_i(x, y)]\}.$$

The open map is the large-scale component of the original map, with the very useful property that at each position,

$$o_N[S_i(x, y)] \leq S_i(x, y).$$

Finally, we construct a filtered map,  $f_N[S_i(x, y)]$ , where

$$f_N[S_i(x, y)] \equiv S_i(x, y) - o_N[S_i(x, y)],$$

and  $f_N[S_i(x, y)] \geq 0$ .

With this straightforward transformation, we now have two maps,  $o_N[S_i(x, y)]$  and  $f_N[S_i(x, y)]$ , which contain the large- and small-scale structure from the original map, respectively. By construction, these are related by the simple property that

$$S_i(x, y) = o_N[S_i(x, y)] + f_N[S_i(x, y)].$$

Figure 1 shows the open and filtered versions of simple one-dimensional Gaussians. It is important to note that the open map, which contains the large-scale structure, is very different from a convolved map or one created with Fourier filtering techniques. This will be clearer in the examples discussed below.

The above procedure is easily generalized to handle multiple scales. [For simplicity, we now omit the  $S_i(x, y)$  notation.] For example, if one takes  $o_N$  as the input map and performs the opening operation with a larger box size of, e.g.,  $2N + 1$ , then a second filtered map can be formed from

$$f_{N, 2N+1} \equiv o_N - o_{2N+1}[o_N].$$

The original map can then be recovered as

$$S_i(x, y) = f_N + f_{N, 2N+1} + o_{2N+1}[o_N].$$

In the following sections, we will discuss the quantitative reliability of filtered maps and spectral indices derived therefrom. To keep this in context, readers should note that the other methods for measuring spectral indices often have even larger

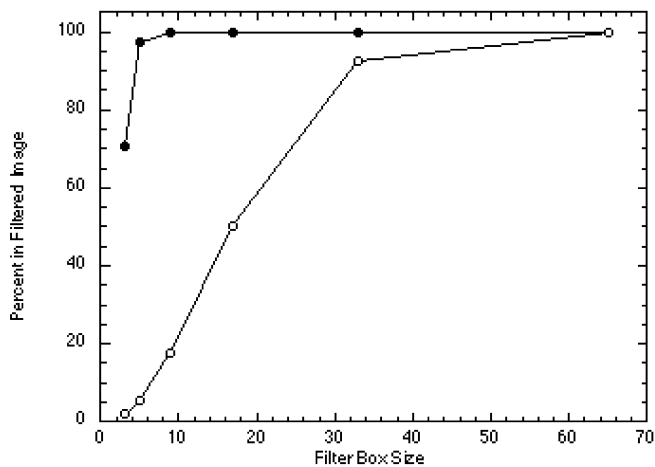


FIG. 2.—Percent of flux appearing in the filtered map as a function of filter box size, for two different Gaussians (filled symbols: FWHM = 3; empty symbols: FWHM = 24).

biases that are typically not treated quantitatively. These include confused spectra from overlapping features in direct division, problems with negative bowls in convolution filtering, and the subjectivity of modeling and tomography.

## 2.2. Partitioning of Features into Filtered and Open Maps

The one-dimensional Gaussian examples of Figure 1 show both the power and limitations of this filtering technique. In each case, we show the original, the filtered, and the open versions of the model, using a one-dimensional box size of  $N = 9$  pixels.

In case *a*, a Gaussian of FWHM of 3 pixels, all of the flux is contained in the filtered image, and the open image is zero.

In case *b*, a ramp is added to the Gaussian. Ideally, the filtered map would contain all of the flux of the Gaussian, as above, and the open map would contain all of the flux of the ramp. We see that the filtered map contains most, but not all, of the FWHM = 3 Gaussian; some of its flux remains in the open image (see pixels  $-3$  and  $-4$ ). This shows the dominant shortcoming in this filtering—it assigns some of the flux from small-scale features into the large-scale open map. The magnitude of this “error” is the *gradient* in the background emission across the full width of the small-scale feature.

A second problem, although this is readily accounted for, is edge effects. If the flux extends all the way to the edge of the map, then some of the large-scale portion of the flux can be partitioned into the filtered map (see, e.g., pixels 13–15). To avoid this problem, all maps to be filtered should contain a buffer region of amplitude zero and size equal to or greater than the box size  $N$ .

Two FWHM = 3 Gaussians with centers separated by

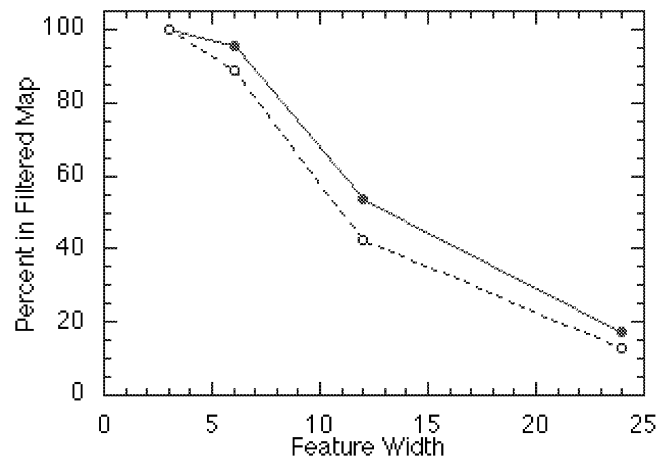


FIG. 3.—Percent of flux appearing in the filtered map with box size 9 pixels, as a function of source size, for both circular Gaussians (filled circles) and highly elliptical (major axis = 100) Gaussians (empty circles).

4 pixels are analyzed in part *c*, forming a feature with an effective width of  $\approx 7$  pixels. The filtered map contains 94% of the flux, while 6% remains in a flat plateau in the open map. In essence, this is what the filtering process is intended to do, namely, to have a fall-off in response to features of increasing size. Part *d* shows a more extreme example, the response to a Gaussian of FWHM = 16. Here, only 24% of the flux is contained in the filtered map.

The response of two features to filters of different sizes is shown in Figure 2. In the ideal case (i.e., with no noise or interference from other structures) the filter box size can therefore be chosen to pass structures of desired sizes (with some leakage of other sized structures). Figure 3 shows the percentage of flux in the filtered map of box size 9 for features of different sizes. This is the box size used in the current paper. We show the response both to circular Gaussians and to highly elliptical Gaussians (major-axis FWHM = 100) as an approximation to long, linear features.

Given that the percentage flux in the filtered map is a function of the feature size, it is *not* appropriate to use the filtered maps as an accurate measure of the total flux of a “feature,” except for features with widths much smaller than the box size, when 100% of the flux will be in the filtered map. To first order, a good estimate of the spectral index of the feature is still possible when the feature width is comparable to the box size, e.g., if only 90% of the flux at each of the two frequencies appears in the respective filtered maps. However, if there are different large-scale gradients at the two frequencies, the filtered maps can contain a small bias, as shown in Figure 1*b*. If one is interested in measuring spectra for features with a wide range of spatial scales, a more extensive multiresolution scheme should be used.

It is important to recognize the difference between “open” maps that show the large-scale structure and maps convolved

to a low resolution. First, convolved maps contain contributions from the small-scale structures; their flux is *not* included in open maps. At a more subtle level, however, the open maps are not “smeared” versions of the original map; any pixel that had zero flux in the original map will have zero flux in the open map. This is true for open maps even if adjacent pixels have considerable flux; it is not true for convolved maps. Thus, the open maps do not *create* large-scale structures; they will preserve, e.g., the sharp edges of otherwise diffuse features. This property also distinguishes multiresolution filtering from Fourier techniques, since the latter incorporate only any sharp edges into the fine-scale structure.

A word on image normalization is in order. The filtering procedure does *not* change the “beam size,” so that flux densities that are quoted in mJy beam<sup>−1</sup> will retain their original scaling in the filtered and open maps. Again, by definition, the total flux is preserved in the sum of the filtered and open maps.

A few other idiosyncrasies of the filtered maps are worth noting. The first, and most obvious, is the appearance of “boxes” in the filtered maps corresponding to the filter box size. These result from the flat-topped nature of the top-hat filtering scheme and clearly do not represent intrinsic source structure. Although one must be careful not to interpret features that are due to the boxy nature of the filtered maps, these also offer an advantage because they are so recognizable. Other filtering techniques also produce residual patterns; if these are smooth, they would not be noticed—although they should be.

Next, sharp negative features (smaller than the box size) will *not* be partitioned into the filtered map as sharp positive features are; negative ones will remain in the open map. This basic asymmetry must be kept in mind during interpretation of any filtered images. Finally, there is an artifact that appears in filtered maps that is too faint to be seen in any of the simulations or actual maps shown here. A source with both dimensions larger than the filtering box will have some of its flux partitioned into the filtered map. (The one-dimensional analog of this is seen in Fig. 1*d*.) In addition, there will be a low-level crosslike structure extending horizontally and vertically from the peak. This is most likely due to the presence of a “pseudo-ridge” in the square filtering box because not all of the pixels in the box are equidistant from the peak. Such features are easy to recognize in filtered maps (looking like diffraction spikes) and do not affect any of the results discussed here.

### 2.3. Filtering Images with Noise

We now explore the propagation of noise into the amount of flux recovered in the filtered maps as a function of feature size. This is an issue because the filtering is not a linear, mean zero response to the input. We started with a map containing 204 circular Gaussians, each with FWHM = 3, and fluxes of 2, 4, 8, and 16. To this map we added Gaussian noise of unit variance, convolved with an FWHM = 3 Gaussian. Before

filtering we forced all negative values in the image to zero, to avoid a bias due to the minimum-searching nature of the algorithm. We also created an amplitude zero buffer equal to the box width to eliminate the edge problems discussed above.

We then filtered this forced positive map using the above algorithm and compared the *actual peak* of the Gaussian ( $P_{\text{actual}} = \text{model} + \text{local input noise contribution}$ ) to the *filtered peak* ( $P_{\text{filtered}}$ ). A least-squares fit showed

$$P_{\text{filtered}} = (1.0 \pm 0.0002)P_{\text{actual}} + (-0.0027 \pm 0.0023).$$

The recovered flux is thus an excellent measure of the actual flux. The rms variations, even at this extremely low level, were dominated by only seven points of 204. The largest residual was 0.17 (with an input rms noise of unity), and the seven large residuals occurred at a variety of actual peak heights. The residuals of the other 197 points had an rms of only 0.0005. We therefore conclude that, except for a few percent possibility of an error of up to 0.17 times the input rms noise, the filtering procedure itself adds no errors to the flux determinations of small, isolated Gaussians.

We now repeat this procedure using the same filter box size but for Gaussian “signals” of FWHM 6, where we expect only 94% of the flux to be recovered. A least-squares fit now yields

$$P_{\text{filtered}} = (0.937 \pm 0.004)P_{\text{actual}} + (0.17 \pm 0.04).$$

We therefore recover the relationship found in the noise-free case, although there is a small bias ( $\frac{1}{6}$  of the input rms noise) in the filtered peak values. This results from the forced positive definite nature of the noise. The overall rms residual from the above relationship is 0.34; for the brightest peaks alone, the residual rises to 0.56. These residuals are significantly less than the irreducible input rms uncertainty of 1.0 for each signal, which comes from the unknown (except in this simulation) noise level at the location of the peak.

We repeat the procedure once again, with 102 Gaussians of FWHM 12. Now we obtain

$$P_{\text{filtered}} = (0.45 \pm 0.01)P_{\text{actual}} + (0.78 \pm 0.1).$$

The residuals have an rms of 1.3 (corrected back to the original map scale) and a bias on the order of the rms input noise. Since these numbers are now comparable to the errors introduced from the local noise alone, the filtering procedure becomes less useful quantitatively. Based on these experiments, we conclude that the filtering is most useful when greater than 90% of the flux of the small-scale feature of interest is recovered in the filtered map. If a feature has a significant amount of flux left in the open map, then the filtering procedure can become an important source of error. Since the procedure conserves flux, an “error” in the filtered map reflects different amounts of flux that are left in the open map.

In the discussion that follows, we will primarily focus on the spectral indices of features that are significantly smaller than the filter box size, and therefore reliable, and features in the open map where only minor contamination from small-scale features is present. Some features in the radio sources studied here probably fall into the intermediate size category, and their measurements must be treated with some caution. Consistency of spectra across contiguous boxes provides one way to assess their reliability. The signatures of filtering errors are discussed in the next section.

#### 2.4. An Extragalactic Source Simulation

In order to examine a more realistic situation than the above Gaussian simulations, we created a model radio galaxy, which is shown in Figure 4. The model was constructed at two frequencies, separated by a factor of 3. It consists of a “hot spot” (circular Gaussian of FWHM = 3 and a spectral index of 0.5), a “jet” ( $3 \times 100$  Gaussian, with spectral index 0.7), a “filament” ( $3 \times 70$  Gaussian, with spectral index 1.0), and a “lobe” consisting of a series of overlapping Gaussians, with spectral indices from 1.0 to 1.4, mimicking the large-scale spectral index gradients seen in radio galaxies. Gaussian noise, convolved to FWHM 3, was then added independently at each frequency.

The source was filtered with a box of width 9, as described above. Figure 4 shows the model source at a single frequency, with its filtered and open maps. Figure 5 shows a one-dimensional slice through these maps, at the location indicated in Figure 4. Note that the filtering process performs exactly as expected, separating out the small-scale structures, both “real” (jet and filament) as well as those coming from noise either on or off source. The one obvious “mistake” made by the filtering process is that it leaves artificial step functions in the open map at the location of the small-scale features. This is what was seen in the ramp of Figure 1*b* earlier, and the magnitude of these “errors” in both filtered and open maps is of order the gradient across the small-scale feature.

Figure 6 shows the error in spectral index determined using the filtered images, as a function of the signal strength. For comparison, the solid line shows the expected rms range in the spectral indices expected from the noise alone if we had not known its simulated value at each point. The major problem visible here is the bias toward flatter spectral indices seen especially for the low flux densities. This problem is important primarily on the *boundaries* of the narrow features in the filtered map. At the lowest flux densities, the bias is strongest along the boundaries of the jet. The cause of this bias is the step-function nature of the open map, which removes from the filtered map the *maximum* of the levels around the base of the small-scale feature; when there is a gradient across the small-scale feature, too little flux remains in the open map, except at the high edge. If the spectral index of the large-scale emission were the same as that of the small-scale feature, then no problem would exist, since the maps at both frequencies would be

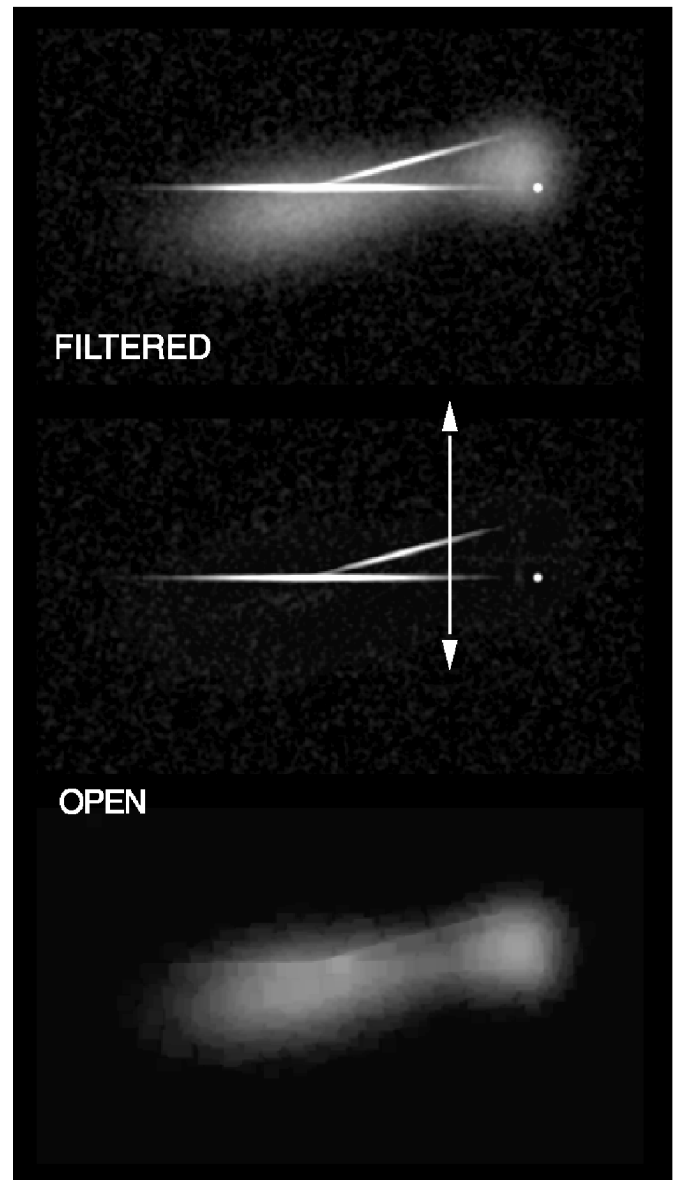


FIG. 4.—Gray-scale image of model extragalactic source, with filtered and open images. The arrow indicates the location of the slice shown in Fig. 5.

equally biased. If the spectral index of the large-scale emission is steeper than the small-scale emission, then relatively more flux goes into the open map at the lower frequency, biasing the small-scale spectra to be flatter along the boundary where the background is lower.

The bias can easily be calculated if the relative strengths of the small-scale feature and the large-scale gradient, and their respective spectral indices, are known. However, it is difficult, in practice, to automatically calculate the biases across an entire map. Happily, there is a clear signature when this problem arises, namely, a sharp gradient in the spectral indices across the small-scale features. In the applications to actual radio gal-

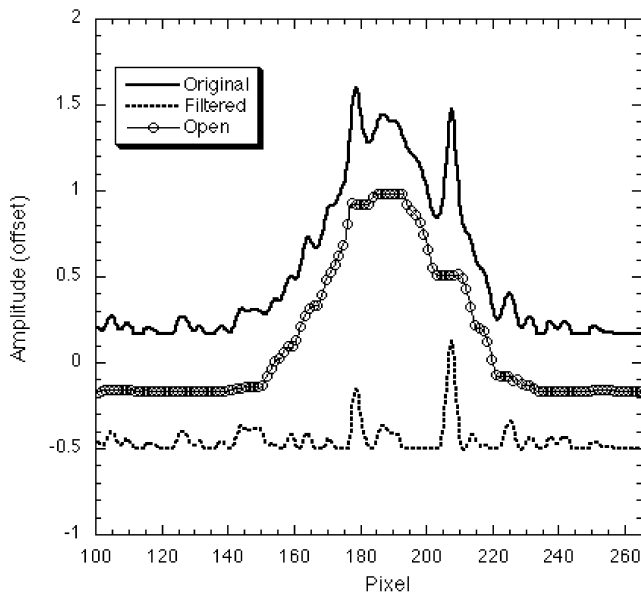


FIG. 5.—One-dimensional slice through model map showing separation of small- and large-scale features in the filtered and open images, respectively.

axes and SNRs described below, we will be attentive to the possible presence of this bias signature.

### 2.5. Summary of Reliability Issues

The multiresolution filtering technique is reliable and useful for isolating features in a map that are smaller than the chosen box size(s). In this situation, it contributes uncertainties and biases that are only a small fraction of the rms noise. With the appropriate care, it can be used as a reliable technique for measuring spectral indices of small-scale features in the presence of varying backgrounds of different spectral indices. The open maps can also provide reliable spectral indices for large-scale emission, providing one ensures that there is only little contamination from intermediate-scaled features.

For features of sizes comparable to or slightly larger than the box size, only a portion of the feature will be partitioned into the filtered map. This is still useful for spectral index work, since the same partitioning will occur at both frequencies, to first order. However, under these conditions, the filtering procedure becomes an important additional source of error, comparable to the rms noise.

In the presence of gradients in the background, small-scale features may show spectral gradients across them. The spectra at the boundaries of the small-scale features are then unreliable because of the bias from the larger scale gradients. These must be treated with caution.

For sources where multiple scales are to be studied, a number of box sizes may be used. Since some features will appear at more than one filtering level, the robustness of spectral determinations should then be examined as a function of filter box

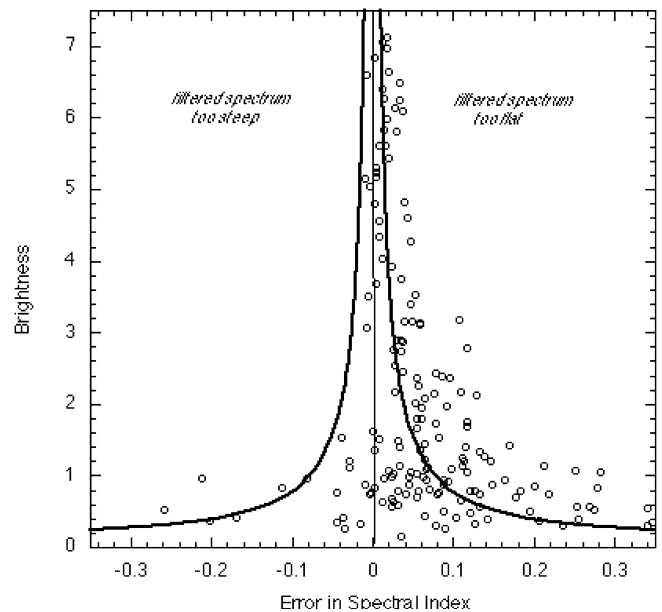


FIG. 6.—Error in spectral index from filtering process, as a function of signal strength. Most of the points outside the expected rms error are from the edges of the jet.

size. This will identify not only potential filtering errors but the more important situations where there is an intrinsic gradient in spectral index across a feature and therefore not a unique “size” that is independent of frequency.

### 3. APPLICATION TO RADIO GALAXIES

For the initial application of the multiresolution filtering method, we selected four FR II sources, based on the existence of some substructure in their lobes and the availability of high-quality matched-resolution maps at two frequencies. Two of the sources, 3C 401 and 3C 438, are analyzed by Treichel et al. (2001, hereafter T01) using the spectral tomography technique. Their small-scale structure is dominated by their jets and filaments in the hot-spot regions. We also chose two sources with weaker jets, 4C 11.14 and Cygnus A, which offer the opportunity to examine other smaller scale features found in their lobes.

The original references to the maps are as follows: Hardcastle et al. (1997), at 8 GHz: 3C 401, 3C 438, 4C 14.11; Leahy et al. (1997) at 1.5 GHz: 3C 401, 3C 438; Leahy & Perley (1991) at 1.5 GHz: 4C 14.11; Carilli et al. (1991) at 1.4 and 5 GHz: Cyg A, with data coming mostly from the Very Large Array (VLA)<sup>1</sup> supplemented by MERLIN<sup>2</sup> data at higher resolution.

Gray-scale images of the original, filtered, and open maps

<sup>1</sup> The VLA and National Radio Astronomy Observatory are facilities of the National Science Foundation, operated under cooperative agreement with Associated Universities, Inc.

<sup>2</sup> MERLIN is a national facility operated by the University of Manchester on behalf of the UK Particle Physics and Astronomy Research Council (PPARC).



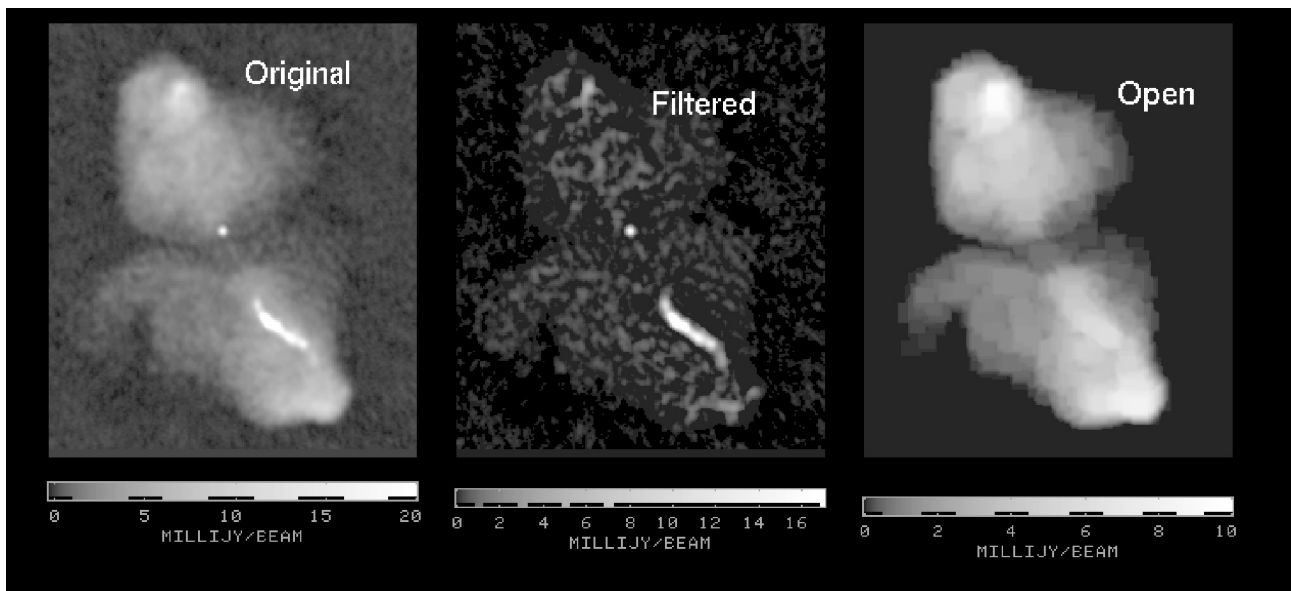


FIG. 7.—Gray-scale total intensity image of 3C 401 at 1.5 GHz, at  $0''.35$  resolution, along with filtered and open maps.

for each source are presented in Figures 7–10. Color images of the spectral distributions in these sources are shown in Figures 11–14 as described in more detail below. Figures 15–18 show the run of spectral indices along the major axis for the original, filtered, and open maps.

### 3.1. Prominent Jet Sources: 3C 401 and 3C 438

Hardcastle et al. (1997) describe both of these sources as unusual for FR II radio galaxies because of their low polarization, prominent jets, and diffuse hot spots. A more detailed discussion of the jet spectra and other properties is given in T01.

Gray-scale images of the 1.5 GHz total intensity and the filtered and open images of 3C 401 and 3C 438 are shown in Figures 7 and 8, respectively. The corresponding maps at

8 GHz were used to construct the spectra shown in color in Figures 11 and 12. In these images of the spectra, we show the spectra from the unfiltered maps as they are usually measured from direct division. For comparison, we show the spectra from the open maps, which differ very little from the unfiltered maps, because the small-scale features do not dominate the emission at most locations. The spectra from the filtered images and a spectral difference map, as discussed below, are also shown.

The spectral difference map, in the lower right corner, provides an important diagnostic for extragalactic radio sources. It is constructed by subtracting from the spectral index of the filtered maps the *local values of the spectra* from the corresponding original maps. Emission from diffuse lobes is typically seen to steepen with distance from the hot spots, com-

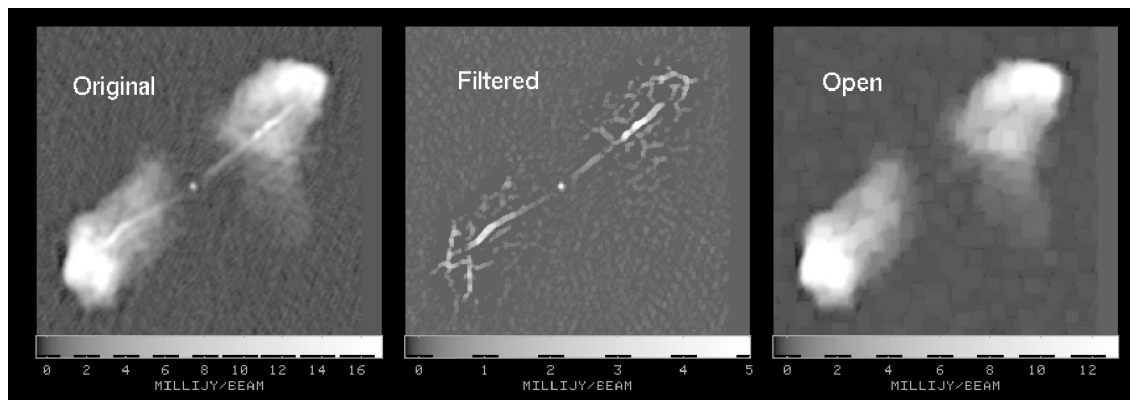


FIG. 8.—Gray-scale total intensity image of 3C 438 at 1.5 GHz, at  $0''.29$  resolution, along with filtered and open maps.

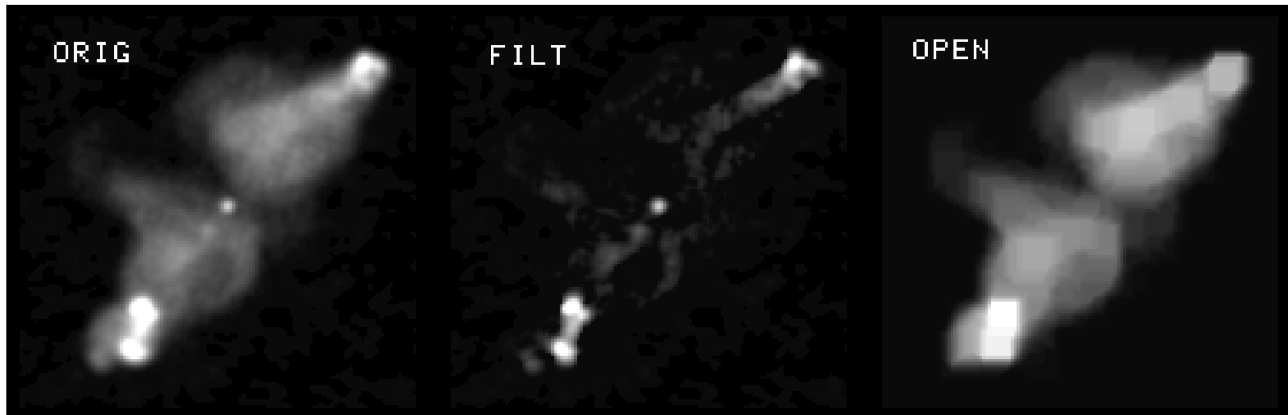


FIG. 9.—Gray-scale total intensity image of 4C 14.11 at 1.5 GHz, at 3'' resolution, along with filtered and open maps.

monly interpreted as a result of progressive synchrotron losses, although weaker magnetic fields downstream are a viable alternative (Rudnick 1999). Where the differences between the small and large-scale spectra are significant, we can ask what physical conditions are responsible. In the case of the jets in 3C 401 and 3C 438, there is a standard explanation, namely, that the jets are assumed to represent outgoing material. The flatter spectra reflect the fact that they have not experienced significant radiative losses or that they undergo continuing relativistic particle acceleration.

However, there are spectral variations in the 3C 438 jet that are not expected in the standard models, as discussed in T01. We also note the presence of locally flatter emission in other small-scale *nonjet*, *non-hot-spot* features, especially in 3C 438. In the north, this appears to be a young post-hot-spot flow that has not experienced significant losses. In the south, the small-scale features do not show any relationship to the hot spot and therefore must arise from some other hydrodynamic source yet still show flatter spectra than the locally surrounding emission. This type of behavior is seen in recent MHD simulations with cosmic rays, where the relativistic electrons visible at any one time and place reflect a variety of acceleration and loss histories and not simply the local conditions (Tregillis, Jones, & Ryu 2001).

As a check on the robustness of our spectral determinations from filtered maps, we compare the jet spectra determined here with those determined via tomography in T01. In Figure 19 we plot these spectra as a function of distance from the cores. The filtered spectra are the median of the values across the jet at that core distance. The median was used to reduce the effects of any gradients due to the background bias, as discussed above. The errors are formal ones only and do not reflect the possible biases noted in the discussion above. The noise was taken, here and in later plots of filtered spectra, from the *on-source* rms, which is significantly higher than the off-source noise and is appropriate

to measuring spectra in the presence of confusing structures. There is also a small gradient in the filtered spectrum across the 3C 401 jet. No correction has been made for the small probable bias caused by the edge effects discussed above; this does not affect any of the discussion here, especially given our use of median spectral values at each location along the jet.

The agreement between the two sets of results is excellent, providing a consistency check for both of these spectral determination methods. There are a few isolated points where there is a significant difference in the results of the two methods. Although the filtering technique is done blindly, T01 had independently noted problems at these locations, e.g., due to confusion from other substructure in the lobes, while doing the tomography analysis.

Comparisons of the trend in spectral index for the filtered, unfiltered, and open maps along the major axis of the source are shown in Figures 15 and 16. Again, we used the median value at each distance from the core. Errors in the open spectra are calculated from the off-source rms, and the images show no indications of possible biases.

In both sources, the unfiltered and open spectra are very similar, as also seen in the color images. The only significant differences occur where the unfiltered images near the core show spuriously flat spectra because of contamination by the jets. Errors in the unfiltered spectra are not shown; they are formally less than or equal to those of the open spectra but are subject to confusion from the different local spectral index of small-scale overlying emission.

In contrast, the filtered and open spectra show quite different behaviors, as expected and seen in the color maps. The three jets show no significant monotonic gradients with core distance, while the underlying lobes steepen significantly. The astrophysical issues raised by the nonmonotonic jet spectral variations are discussed in T01. In the northern half of 3C 401, the small-scale, nonjet features generally track the spectral

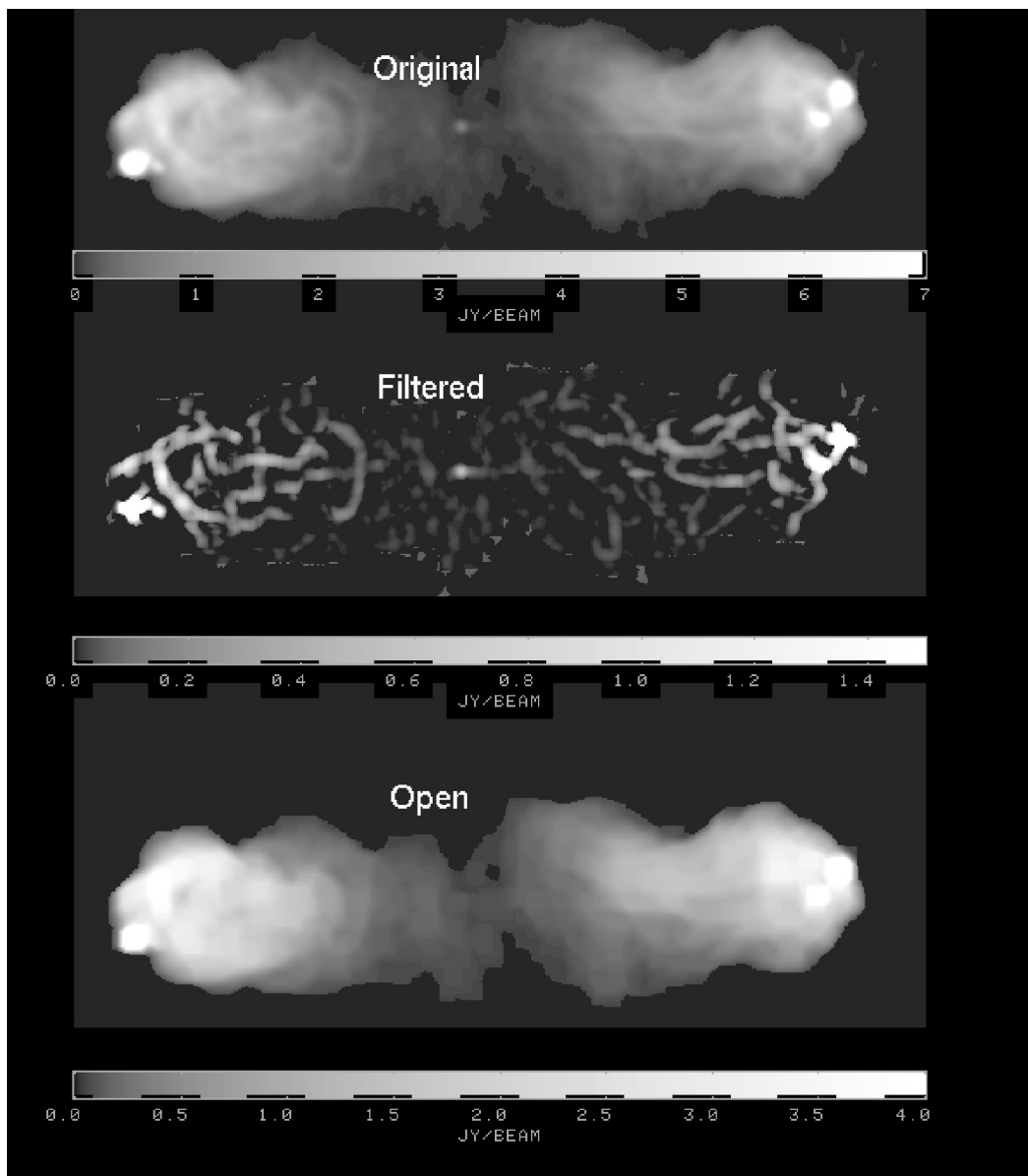


FIG. 10.—Gray-scale total intensity image of Cyg A at 1.4 GHz, at  $1''.5$  resolution, along with filtered and open maps.

trends of the large-scale emission but are generally slightly flatter by about 0.1–0.2.

### 3.2. Weak Jet Sources: 4C 11.14 and Cygnus A

The data for 4C 14.11 are from Hardcastle et al. (1997), who also briefly discuss its spectral behavior and identify the ridge seen in the southeast with a jet, based on the high-resolution map that shows that one component is a linear feature aligned with the core. Our results are consistent with this explanation and are shown, as for the above sources, in Figures 9, 13, and 17. The ridge of emission in the southeast has

a significantly flatter spectrum, as seen in the filtered maps, than the surrounding emission.

The situation in the northwest represents a different phenomenon. While a ridge of emission also appears in the filtered map, the small-scale emission does not connect or point clearly to the nucleus. In addition, there is some small-scale emission quite far from the major axis. All of these regions have flatter spectra than the large-scale emission. Although some of this may be due to a jet hidden by lobe confusion, some of it must be nonjet material. The small-scale emission is 0.1–0.2 flatter than its surroundings.

Cyg A has been studied extensively at many wavelengths,

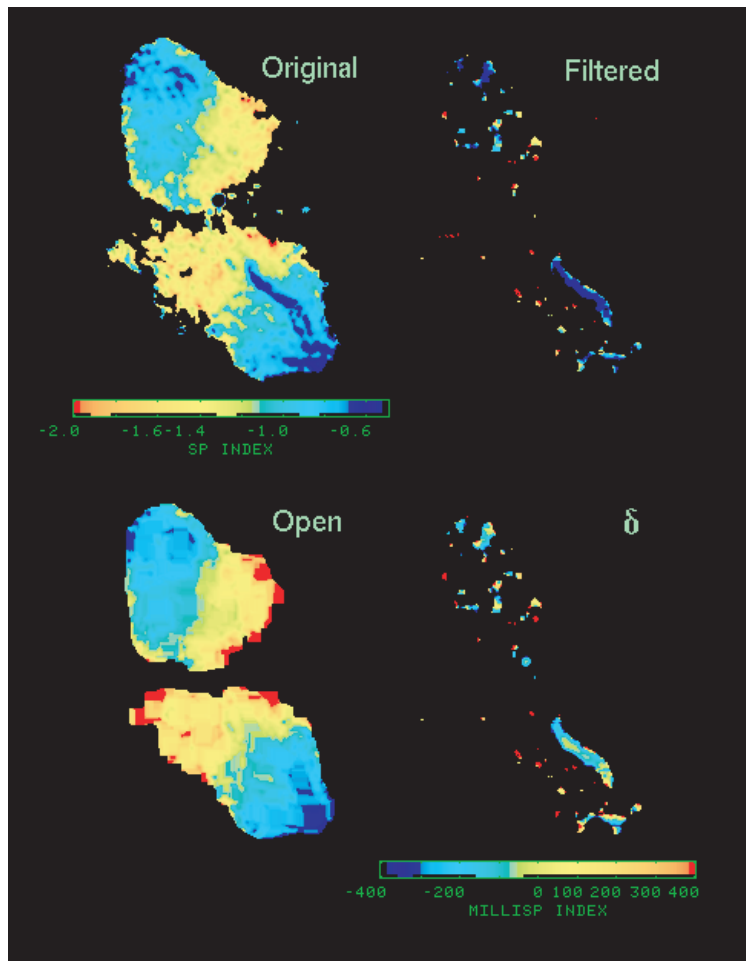


FIG. 11.—Spectral indices for 3C 401. Original: spectral index distribution from the original, unfiltered maps. Filtered: spectral indices from the filtered maps. Open: spectral indices from the open maps. All of the above use the color bar shown with Original.  $\delta$ : difference between the spectral indices of the filtered maps and the spectral indices of the original maps at the corresponding positions. The color bar for this image is below it; blue colors indicate where the filtered map is flatter than the original map.

and the data used here are from Carilli et al. (1991), who also discuss the spectral index behavior of this source. Katz-Stone et al. (1993) and Katz-Stone & Rudnick (1994) performed detailed studies of the spectral variations in Cyg A and noted the presence of overlapping features of different spectra. The multiresolution filtering presented here confirms these results and provides quantitative estimates of the spectra of a variety of small-scale features. Results are shown in Figures 10, 14, and 18. The beam size is  $1''.5$ , and the pixel size is  $0''.3$ . With 5 pixels  $\text{beam}^{-1}$  instead of 3 for the other sources, the filtered maps for Cyg A contain only 90%–95% of the unresolved feature flux, and there is better rejection of larger scale features. None of this affects our interpretation of the results.

Both lobes of Cyg A contain rich substructures, whose spectra are typically flatter than the surrounding material. In the eastern lobe, the small-scale features are typically 0.3 flatter, with significant variations, and tend to follow the overall steep-

ening trend of the large-scale emission. In the western lobe, the small-scale features follow the large-scale trend but are flatter by about 0.1 near the hot spot. However, farther back in the lobe, the small-scale features show no further steepening and become greater than 0.5 flatter than the diffuse emission. There are significant exceptions to this behavior, however; features that are transverse to the major axis in both lobes are somewhat *steeper* than their surroundings.

#### 4. RADIO GALAXY RELATIVISTIC PARTICLE EVOLUTION

The varieties of spectral behavior uncovered here do not fit into any simple model of extragalactic radio sources. As shown by Jones, Ryu, & Engel (1999) and Tregillis et al. (2001), the postjet, post-hot-spot emission contains a mixture of spectral indices because of the particles' respective histories of shock

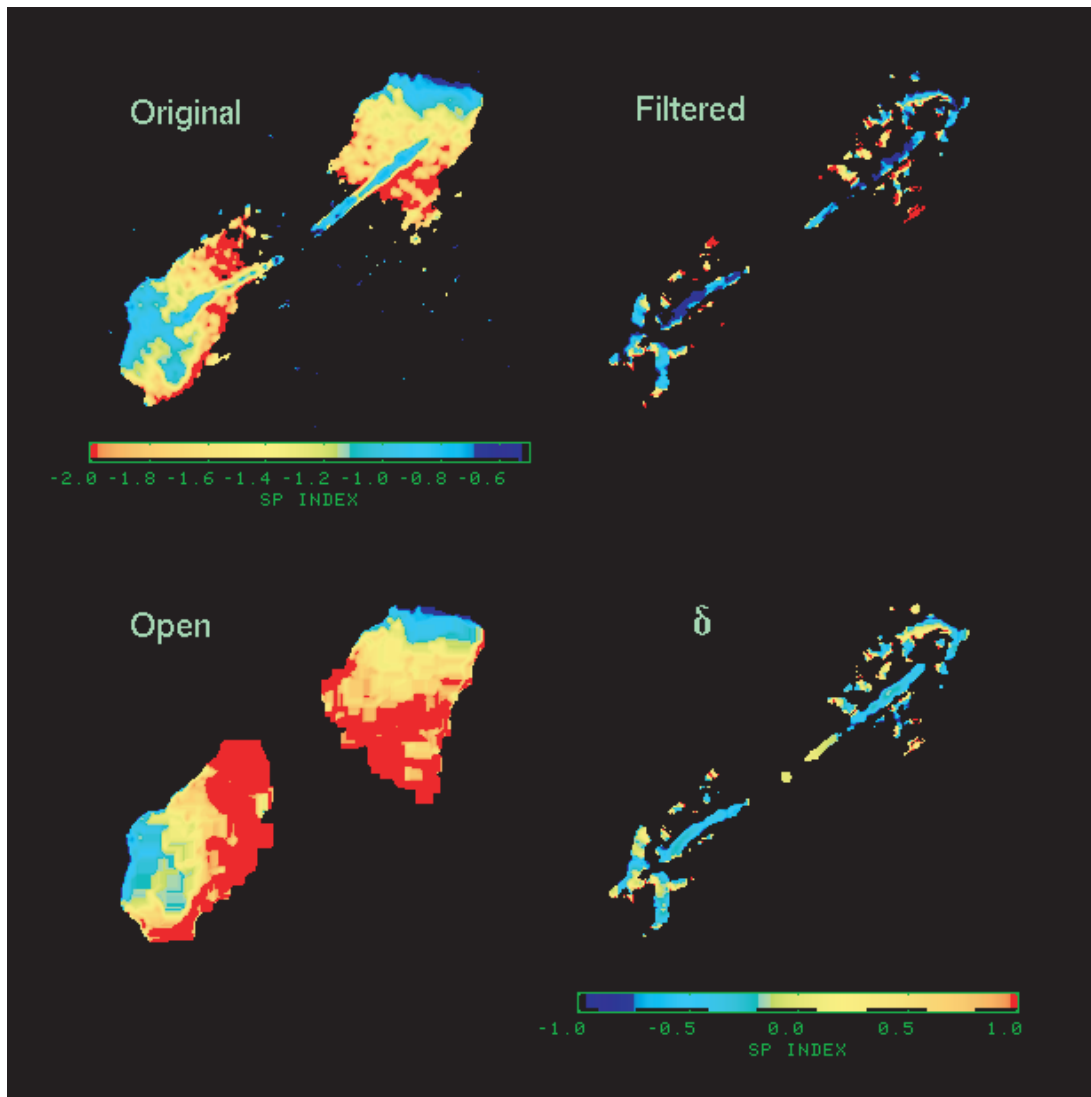


FIG. 12.—Same as Fig. 11 but for 3C 438.

passage, radiative losses, etc. Further progress depends on being able to understand, for a given observed feature, what the probable history of its relativistic electrons has been. Three-dimensional MHD simulations that also treat the relativistic particles properly will make a major step in this direction.

We can use the present results to identify questions for future study. The jets and hot spots show flatter spectra, as expected if they are the sites of recently energized particles. We focus here on the observation that most other small-scale features are also flatter, by 0.1–0.5 in spectral index. Their monochromatic emissivities range from  $\approx 3$  to  $\approx 30$  times higher than their surrounding large-scale emission, although these estimates are clearly dependent on their poorly understood geometry, which we assume here to be cylindrical. In this section, we therefore briefly discuss under what conditions we might see brighter and somewhat flatter features in the presence of lower emis-

sivity, steeper spectrum material. For convenience, we call these small-scale features “filaments.”

The expected variations of emissivity,  $\epsilon$ , with spectral index and frequency are shown in Figures 20 and 21, respectively. These are based on an initially power-law spectrum with a low-frequency index of 0.5 and synchrotron losses with no replenishment by pitch-angle scattering (Jaffe & Perola 1973). Figure 21 also shows the transformations of the spectrum under changes in physical conditions as described below.

*Could the filaments have the same monochromatic emissivity as the surrounding emission at low frequencies but have experienced fewer synchrotron losses?* Such a situation could arise if the filaments are tubes of fast-backflowing post-hot-spot material. In this case, we could assume that the density of relativistic particles (at lower energies) and the magnetic field strength was the same in the filament and its surroundings. When observed

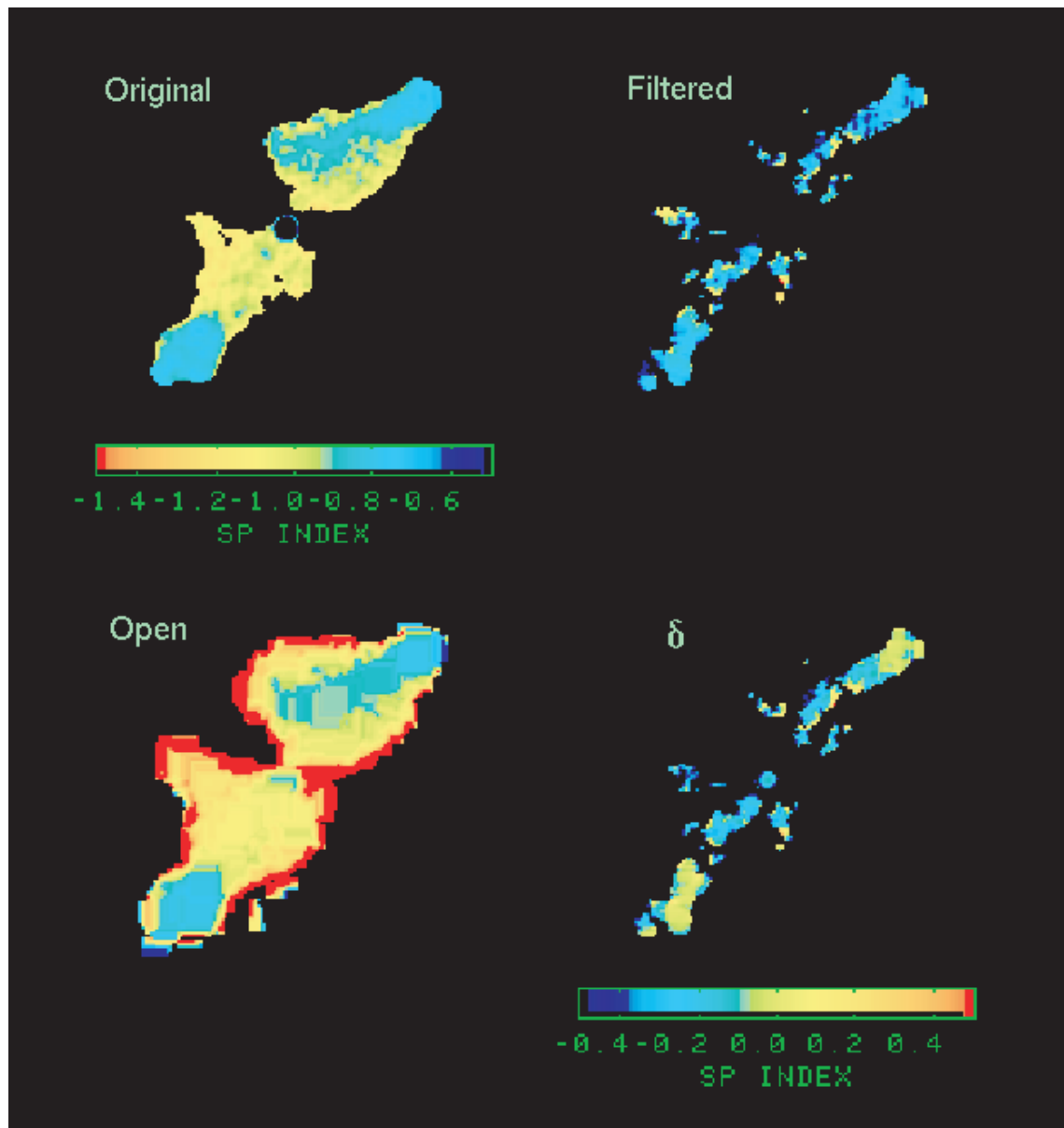


FIG. 13.—Same as Fig. 11 but for 4C 14.11.

at a sufficiently high frequency, the younger (filament) population of particles would then appear both brighter and flatter. However, with reference to Figure 20, we see that a characteristic change in spectral index of  $\approx 0.2$  corresponds to a change in  $\log \epsilon \approx 0.15$ , or a factor of 1.4, much lower than the factors of 3–30 observed here. Unless the filaments actually represent sheets seen edge-on, the observed emissivity change is too high. Therefore, cylindrical populations of particles that are young but otherwise identical to their surroundings (in magnetic field strength and low-energy particle density) are *not* a viable explanation for most of the filaments that appear both brighter and flatter than their surroundings.

An alternative picture is that the filaments represent regions of higher magnetic field. We distinguish between two very different pictures; in the “instantaneous high field” model, the relativistic electrons have just entered the high-field region,  $B_H$ , from the surrounding low-field medium  $B_L$ . The complementary scenario is the “trapped high field” picture, where the relativistic electrons have always been in high fields.

Looking first at the instantaneous high field situation, we assume that the relativistic particles experience no change in density or energy as they enter the high-field region. Then, the observed spectrum will change as shown in the solid arrows in Figure 21. The monochromatic emissivity at a fixed ob-

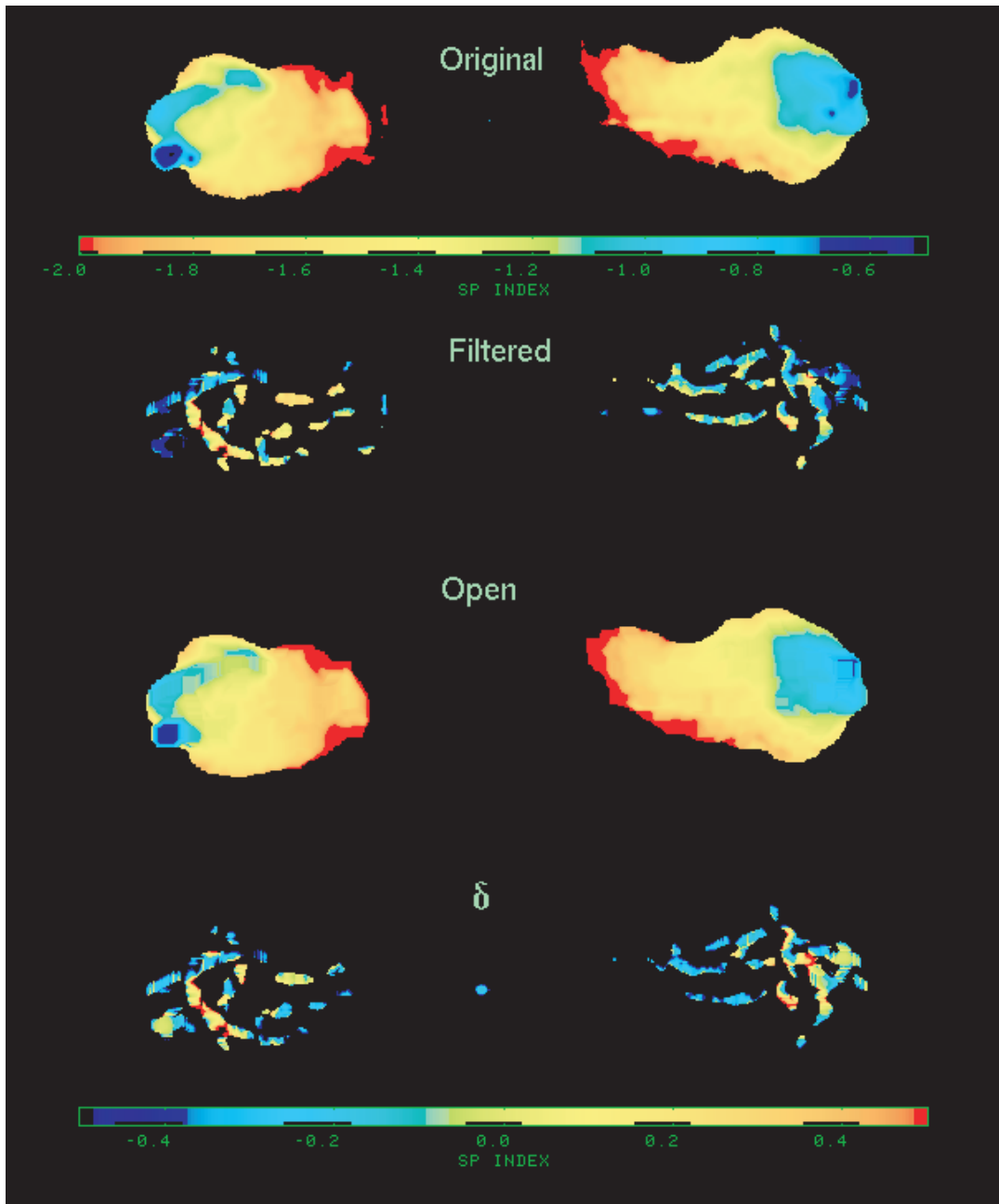


FIG. 14.—Same as Fig. 11 but for Cyg A.

serving frequency changes for two reasons. First, the spectrum is shifted along the  $\log \epsilon$  axis by an amount  $\log (B_H/B_L)$  because of the increased monochromatic emissivity *per particle*. Second, the spectrum is shifted along the  $\log \nu$  axis by the same amount because the frequencies at which each particle radiates are proportional to  $B$ . The total change in monochromatic emissivity at fixed frequency is then

$$\log \frac{\epsilon_H}{\epsilon_L} = [1 + \alpha(\nu)] \log \frac{B_H}{B_L},$$

where  $\alpha(\nu)$  is the value of the local spectral index at the specific observing frequency. In the case of a pure power law,  $\alpha(\nu)$  is a constant. For  $\alpha(\nu) \approx 1$ , a change in spectral index of  $\approx 0.2$  corresponds, as above, to  $\log (B_H/B_L) \approx 0.15$ , so  $\log (\epsilon_H/\epsilon_L) = 0.3$ , again lower than the apparent emissivity ratio of most of the observations. Thus, simply increasing the magnetic fields to flatten the spectrum and increase the emissivity is not a good explanation for the filaments. However, if we were to invoke a higher particle density in the higher field regions, then the high observed emissivities would also be recovered and this model would be viable.

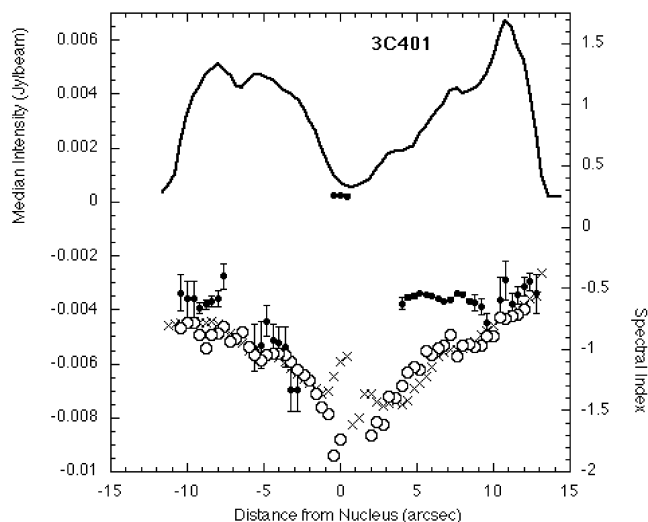


FIG. 15.—Slices along the major axis of 3C 401, with details as described in the text. The solid line shows the total intensity from the original map. The points plotted below show the spectral indices along the major axis determined from the original maps (*crosses*), the filtered maps (*filled circles*), and the open maps (*empty circles*).

Looking now at the trapped high field picture, in addition to the higher emissivity and frequency-shifting effects described above, there are higher losses due to the stronger magnetic fields. The additional effects are shown as dashed arrows in Figure 21. Although the losses simply represent migration of the curved high-energy tail of the spectrum to lower frequencies, in order to express this in the language of shifts in the  $(\log \epsilon, \log \nu)$  plane, we need to use a combination of vertical and horizontal shifts. The spectrum shown in filled circles is that obtained by having a filament that is identical to the surrounding emission except for its magnetic field strength and assuming that the electrons have always been trapped in high fields. Since the cutoff frequency  $\nu_c$  scales according to  $\nu_c \propto B^{-3} t^{-2}$ , the shift along the log frequency axis contains contributions from these losses as well as the change in radiation frequency with field strength. The final relationships, covering all effects, are

$$\begin{aligned} \delta \log(\nu) &= \log \frac{B_H}{B_L} - 3 \log \frac{B_H}{B_L} - 2 \log \frac{t_H}{t_L} \\ &= -2 \left( \log \frac{B_H}{B_L} + \log \frac{t_H}{t_L} \right) \end{aligned}$$

and

$$\delta \log(\epsilon) = \left( \log \frac{B_H}{B_L} + \alpha_0 \log \frac{B_H}{B_L} \right) = (1 + \alpha) \log \frac{B_H}{B_L}.$$

The quantity  $\alpha_0$  is the low-frequency power-law index, and  $t_{H,L}$  represents the time spent in the high- and low-field regions,

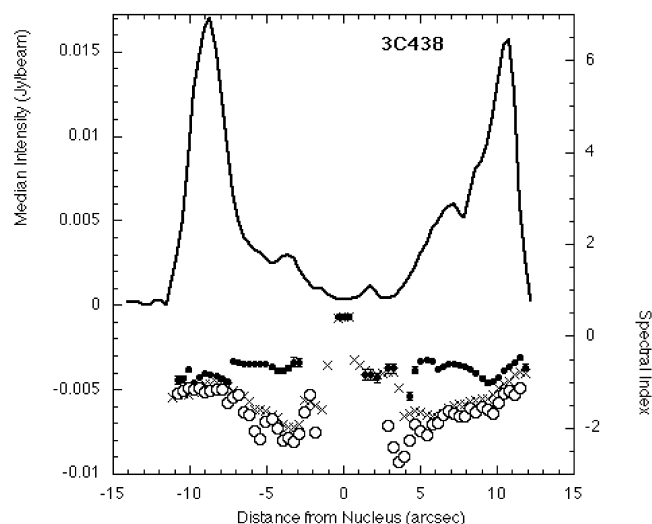


FIG. 16.—Same as Fig. 15 but for 3C 438.

respectively, which we assume to be the same in the example in the figure. For the shifts on both axes, the first term represents the effects of instantaneously being in a different strength field while the next term(s) represent results from synchrotron aging.

Two important results are now apparent for the trapped high field model for filaments, in which particles have been trapped since their initial acceleration. First, the spectra are *steeper* at all possible observing frequencies in the high-field region because  $\delta \log \nu$  is negative and the observations then sample higher energy particles, where the slope is steeper. This is opposite to the nominal expectation that spectra should be flatter in high-field regions because the electron population is being sampled at lower energies. Most filaments we observe *cannot* then represent high-field regions where the particles have been

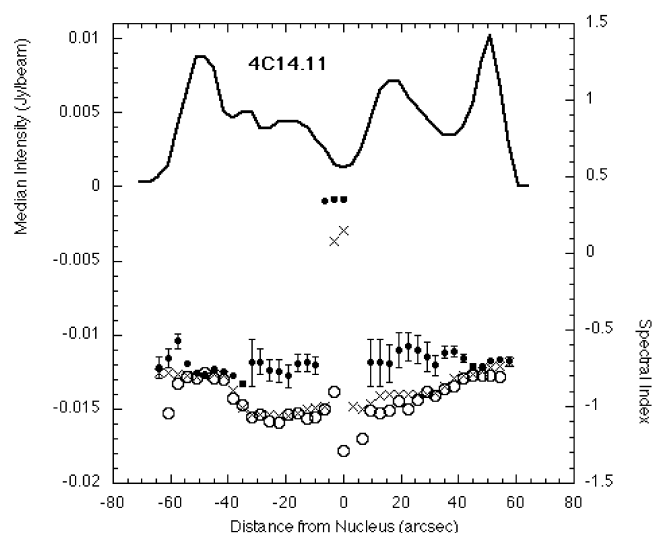


FIG. 17.—Same as Fig. 15 but for 4C 14.11.



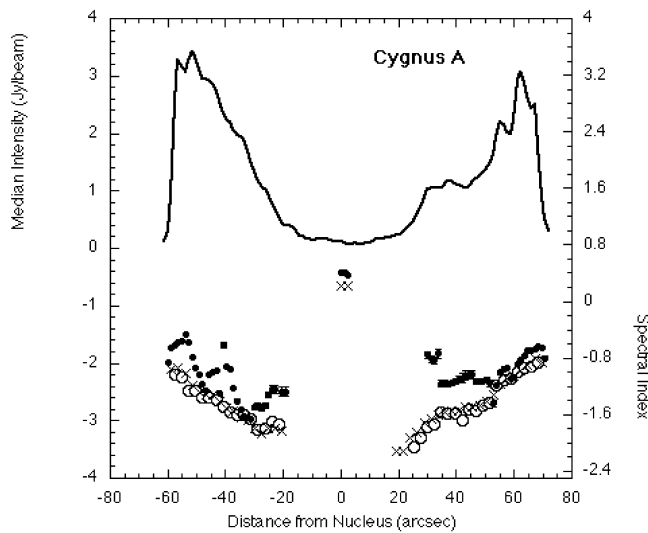


FIG. 18.—Same as Fig. 15 but for Cyg A.

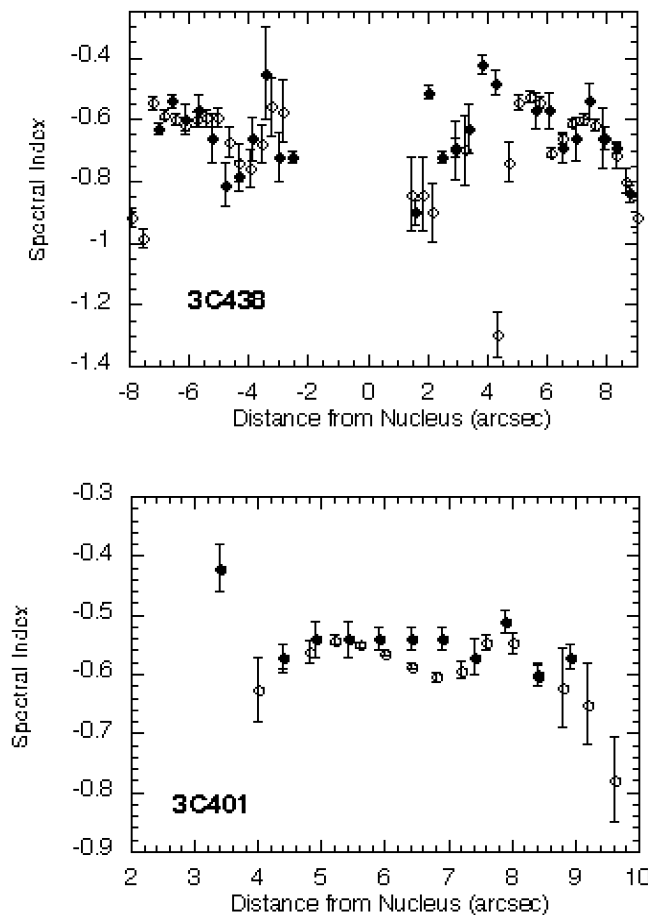


FIG. 19.—Spectral indices for the jets in 3C 401 and 3C 438 determined from the filtered maps, plotted with the respective values from the tomography determinations by T01.

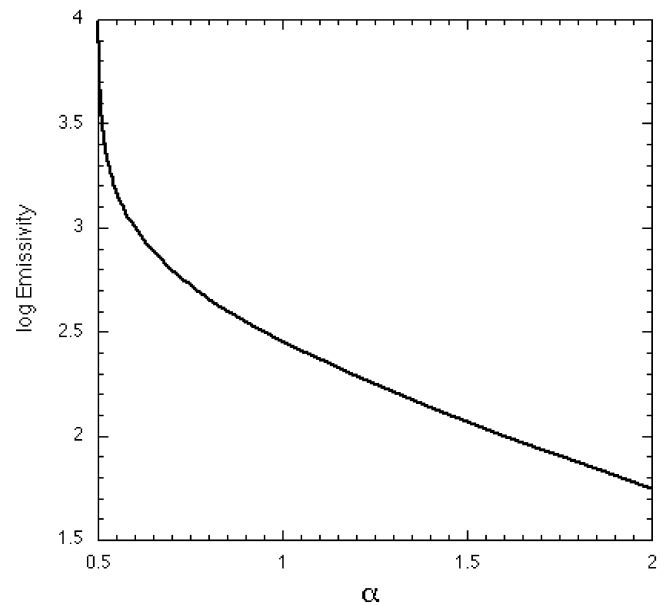


FIG. 20.—Monochromatic emissivity as a function of spectral index for an initially power-law spectrum with an injection index of 0.5 subject to synchrotron losses with no replenishment by pitch-angle scattering.

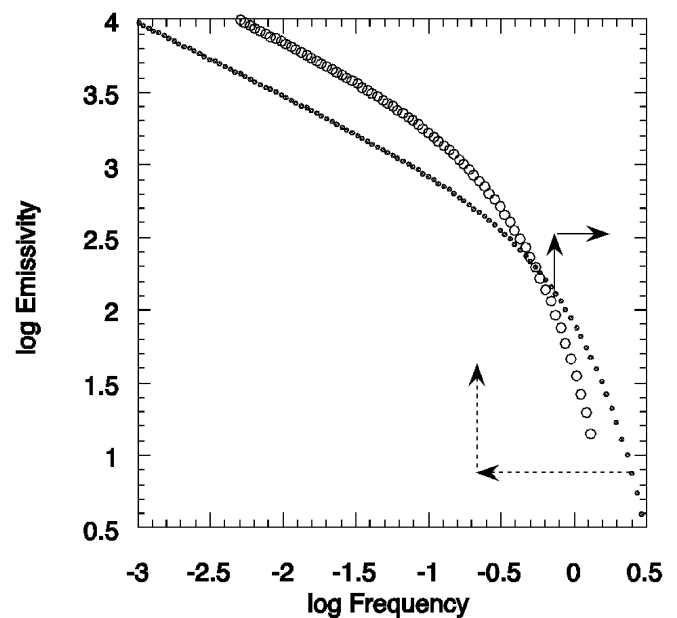


FIG. 21.—Theoretical transformations of observed spectra with changes in magnetic field. The original spectrum is shown as small filled circles. Solid arrows show the effects on the emissivity and radiating frequency of all electrons if the magnetic field is instantaneously increased by a factor of 2.5. The dashed arrows show the additional effects of aging in the increased field, for an arbitrary combination of magnetic field and age ratios, as described in the text. It shows that high-field regions can appear either steeper or flatter, and either brighter or fainter, depending on observing frequency and particle history.

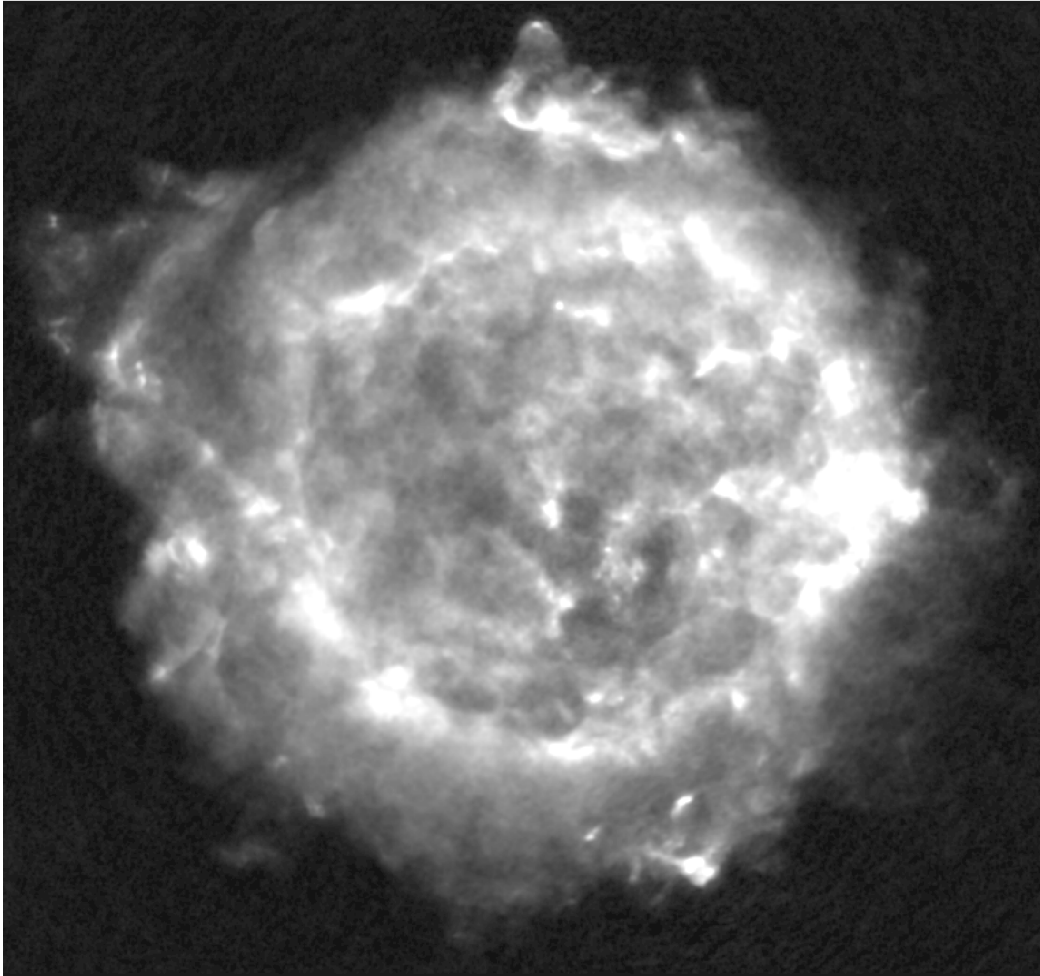


FIG. 22.— $\lambda 20$  cm image of Cas A, at a resolution of  $1''.4$ , from epoch 1994.

present for their entire post-hot-spot life, since we often observe their spectra to be flatter. Second, the monochromatic emissivity can be *either higher or lower* in the high-field region, depending on the observing frequency. Again, this is different from the nominal expectation that higher magnetic field implies higher emissivities. This brings up the interesting possibility that most filaments are actually *low-field* regions, which appear flatter and brighter at high frequencies than their surrounding lobes, because the higher field lobes have experienced greater radiative losses.

The transverse features in both lobes of Cyg A, with steeper spectra than the local diffuse emission, could be higher field regions with particles that have been trapped in them for a long time, yielding the combination of higher emissivities and steeper spectra. At higher observing frequencies, such features would not be easily detectable against the lobe emission. In this context, it would be interesting to look for a population of such structures in radio source lobes, using low frequencies and high resolutions.

The presence of spectral variations outside of the canonical jets, hot spots, and lobes complicates efforts to identify sites of acceleration and loss for the relativistic particle populations. For example, on the loss side, spectral index steepening is the canonical method for assigning ages to radio lobes. However, if the diffuse emission of radio lobes is composed of faint filamentary structures with a covering factor of  $\approx 1$ , then the lobe ages are indeterminate because of the unknown fields and full particle histories.

## 5. APPLICATION TO CASSIOPEIA A SUPERNOVA REMNANT

Cas A is a widely studied SNR, with matched  $1''.4$  resolution maps over its  $5'$  diameter at  $\lambda 6$  cm and  $\lambda 20$  cm (Fig. 22; see, e.g., Anderson & Rudnick 1995, 1996). Because of this wide range in spatial scales, we have decomposed the images at  $\lambda 6$  cm and  $\lambda 20$  cm each into three filtered and one open component, using filtering box sizes of 11, 41, and 129 pixels (at

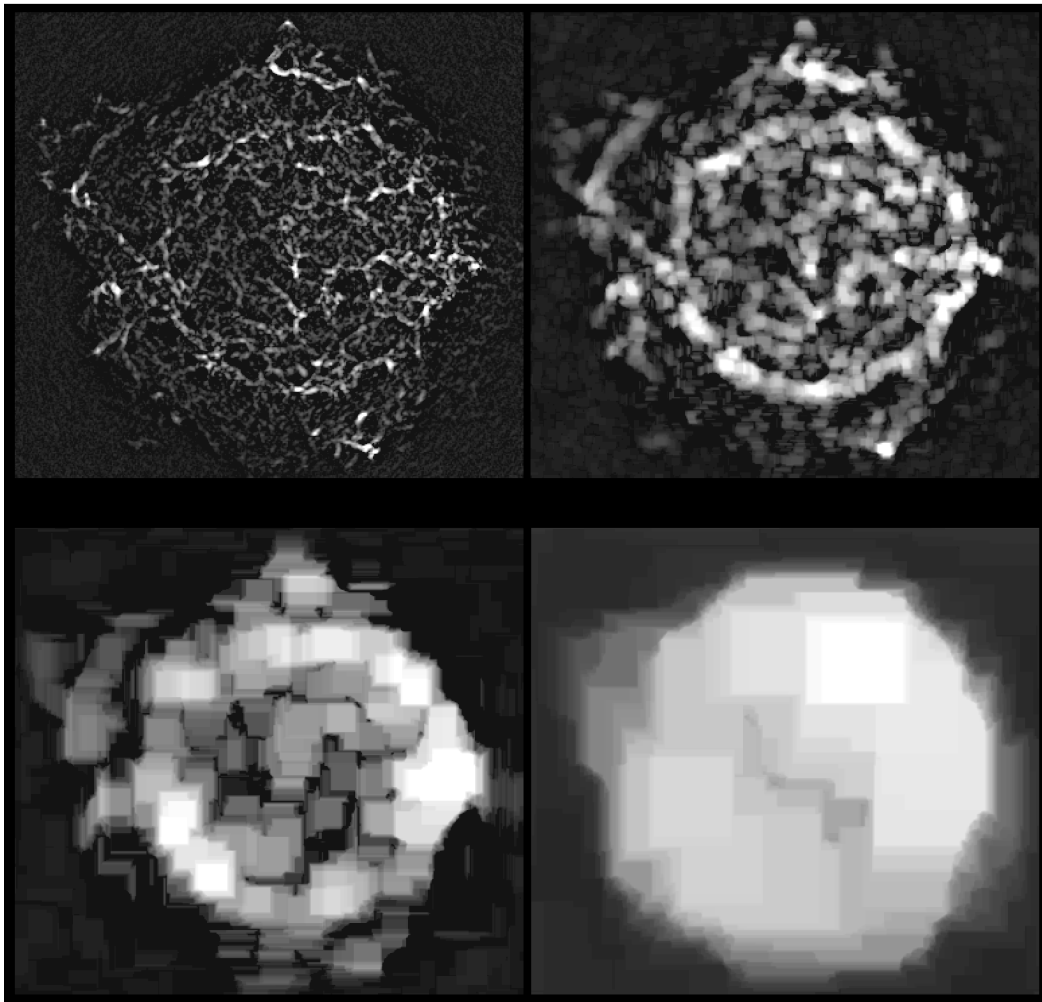


FIG. 23.—Four filtered images of SNR Cas A at  $\lambda 20$  cm, whose sum is equal to the original  $\lambda 20$  cm image. *Top left:*  $f_{11}$ ; *top right:*  $f_{11,41}$ ; *bottom left:*  $f_{41,129}$ ; *bottom right:*  $o_{129}$ . The top two maps show flux densities from 0 to 70 mJy beam $^{-1}$ ; on the bottom the range is 0–50 mJy beam $^{-1}$ .

0".467 pixel $^{-1}$ ). These box sizes were chosen to be relatively well separated and still give a reasonable number of resolution elements across the remnant.

The original map,  $S$ , at each frequency, is therefore decomposed as

$$S = f_{11} + f_{11,41} + f_{41,129} + o_{129}.$$

For this analysis, we used maps from the epoch 1994, with mean frequencies of 4.80 GHz ( $\lambda 6$  cm) and 1.29 GHz ( $\lambda 20$  cm). The filtered maps ( $f_{11}, f_{11,41}, f_{41,129}, o_{129}$ ) are shown for  $\lambda 20$  cm in Figure 23, where the total flux in each map is 158, 463, 542, and 988 Jy, respectively. The off-source rms values are 0.38, 0.25, 0.17, and 0.37 mJy beam $^{-1}$ . The corresponding  $\lambda 6$  cm maps are only subtly different from those at  $\lambda 20$  cm, yielding small but important variations in spectral index across the rem-

nant, as discussed below. The corresponding total fluxes in the four maps at  $\lambda 6$  cm were 65, 172, 200, and 309 Jy. The total reconstructed fluxes are thus 2151 and 746 Jy at  $\lambda 20, 6$  cm, which are 8% and 3% above the Baars et al. (1977) scale, assuming a frequency-independent secular flux decrease of 0.8% yr $^{-1}$  (Hook, Duffett-Smith, & Shakeshaft 1992).

Based on the response functions shown in Figure 3, we can very approximately describe these four images as being dominated by structures on scales less than 5", 5"–20", 20"–60", and greater than 60", respectively. It is important to remember that any physical “feature” can have some signal in two adjacent filtered/open images, although very little of the flux from a feature present, e.g., in  $f_{11}$  should be found in  $f_{41,129}$ , unless it intrinsically has a wide range of scales. Given the similarities between these maps, there are therefore a variety of structures, such as the dominant bright ring, that have a broad range of intrinsic scales. Note that this is *not* the same as finding similar

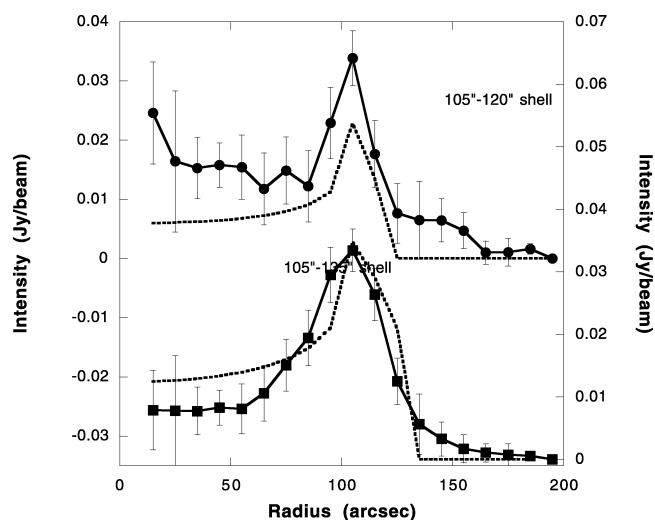


FIG. 24.—Average brightness as a function of radius for the smaller scale emission ( $f_{11} + f_{11,41}$ ; circles) and larger scale emission ( $f_{41,129} + o_{129}$ ; squares), along with uniform emissivity shell models shown as dashed lines, which do not provide good models for the filtered maps, as discussed in the text.

features in maps made at different resolutions, where the apparent large-scale structures can simply be convolutions of small-scale features.

Figure 24 shows an attempt to model the brightness as a function of radius as uniform emissivity shells. This procedure actually fails, as discussed below, highlighting a danger in using two-dimensional filtered maps (of any type) to isolate optically thin three-dimensional structures. We present it here as a warning in the use of filtered images.

The top plot shows the brightness as a function of radius in the smaller scale [ $f_{11} + f_{11,41}$ ] images, while the bottom plot shows the brightness as a function of radius in the larger scale [ $f_{41,129} + o_{129}$ ] images. A uniform emissivity shell from 105" to 120" provides a good fit to the brightness of the ring in the small-scale emission but significantly *underestimates* the brightness at smaller radii. The standard conclusion would be that there is significant emissivity at smaller radii in three dimensions. However, this was a model for the small-scale features alone. When we look at the larger scale emission, we find that the apparently good fit to a 120"–135" shell *overestimates* the brightness at smaller radii. It is possible that there is actually an increasing (decreasing) emissivity of small-scale (large-scale) features toward the center in three dimensions. However, this seems quite artificial, and the above results are more likely to be an artifact of filtering. This apparent problem probably arises because at the location of the bright ring, many small-scale features are seen in projection against each other. Thus, more of the power from the ring is filtered into the large-scale images than from the face, where filaments are more isolated and will be properly filtered into the small-scale images. Thus, although filtered images are a fair representation of different scales of the brightness *on the sky*, they cannot be directly

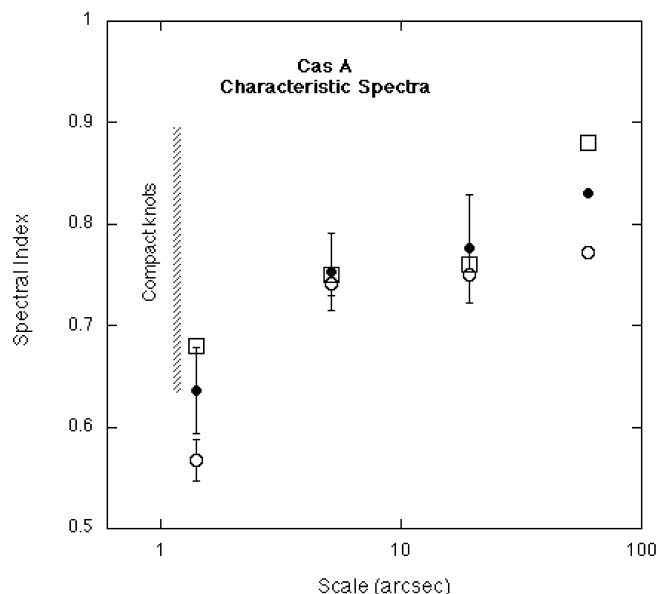


FIG. 25.—Characteristic spectral index as a function of scale size of features in Cas A, with different effective averaging techniques. The points are plotted at the *smallest* spatial scales present in that image. No errors are plotted for the largest scale points, which could be affected by differences in interferometer UV coverage. *Open circles*: Least-squares regression using brightness as a function of radius at both  $\lambda 20$  and  $\lambda 6$  cm. *Filled circles*: Minimizing residuals in scaled difference maps between the two frequencies. *Open squares*: Values from total flux in each filtered image, with errors dominated by calibration uncertainties of order a few percent at each band.

applied, without further assumptions, to represent distinct components in three dimensions. This caveat applies to any filtering method and is important to remember because it may enter interpretations in subtle ways.

Turning now to the spectral behavior, we find the total spectral index to be  $-0.81$ , consistent with the Baars et al. (1977) value of  $-0.77$ , given our likely calibration error of a few percent at each frequency. The spectral indices of the  $f_{11}$ ,  $f_{11,41}$ ,  $f_{41,129}$ , and  $o_{129}$ , given the fluxes as above, are  $-0.68$ ,  $-0.75$ ,  $-0.76$ , and  $-0.88$ , respectively, with errors again dominated by our calibration uncertainties. This thus suggests that the largest scale emission is steeper than the rest. Although it is possible that this is due to missing flux on the shortest (unsampled) baselines at  $\lambda 6$  cm, the total fluxes quoted above suggest that most or all of the flux has been reconstructed. A verification of this result will be possible from comparisons of contemporaneous  $\lambda 50$  and  $\lambda 20$  cm maps, which are currently under analysis.

We examined the spectra on the various scales in two additional ways, both of which are insensitive to any offset biases that could affect the above results (see Fig. 25). First, we made azimuthal averages of the flux in each filtered image at each frequency as a function of radius from the remnant center. Then we performed a least-squares fit of the  $\lambda 20$  cm azimuthal average values against the corresponding  $\lambda 6$  cm values for each

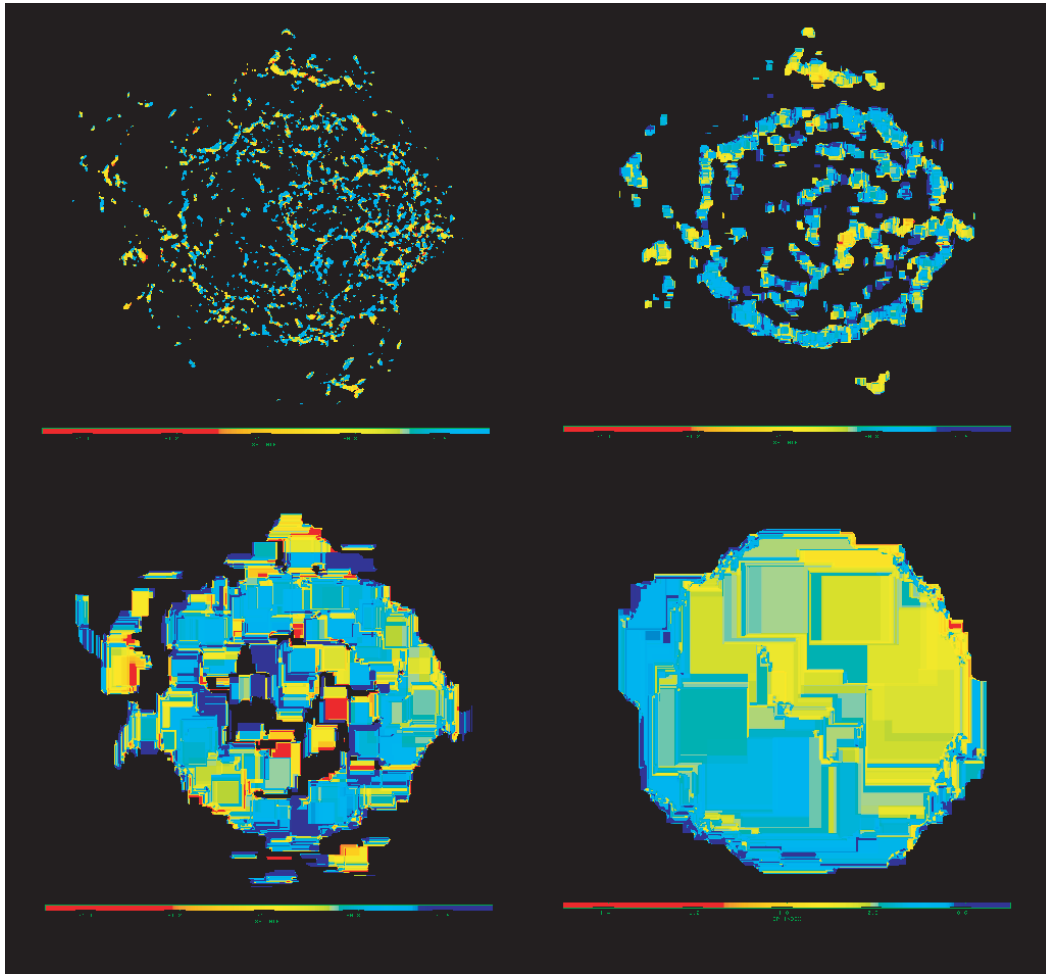


FIG. 26.—Spectral indices for the four maps of Cas A shown in Fig. 23, between  $\lambda_6$  and  $\lambda_{20}$  cm.

filter size. The corresponding spectral values show the same trend toward being steeper at larger scales. The second method was to minimize the quantity

$$\chi^2(\rho) = \frac{(f_{\lambda_{20} \text{ cm}} - \rho f_{\lambda_6 \text{ cm}})^2}{\sigma_{\lambda_{20} \text{ cm}}^2 + \rho^2 \sigma_{\lambda_6 \text{ cm}}^2}$$

as a function of  $\rho$ . The quantity  $\sigma^2$  represents the variance in each image, as opposed to the off-source noise, since actual variations in structure at the two frequencies and spectral index dominate the residuals. The results of this analysis again show the same trends. All of the independent measures of spectral indices at the different scales are shown in Figure 25. We also plotted the observed spectral indices at each scale as a function of intensity. There is little, if any, bias apparent, and the largest scale emission is still steepest.

We performed one other test against a bias of the filtering procedure for different values of signal-to-noise ratio on the  $\lambda_{20}$  and  $\lambda_6$  cm maps. We did this by adding different amounts

of noise to the  $\lambda_6$  cm  $f_{11}$  map, since this smallest scale map showed a different characteristic spectral index from those on larger scales. The original (off-source) noise in the  $f_{11}$  map was  $0.4 \text{ mJy beam}^{-1}$ , yielding a mean spectral index of  $-0.636$ . Increasing the random noise by a factor of 2(4) yielded a mean spectral index of  $-0.648(-0.645)$ . Although the scatter between the two frequency maps increased significantly with additional noise, no bias in the spectral determinations was apparent. We thus conclude that the relative signal-to-noise ratio values between  $\lambda_6$  and  $\lambda_{20}$  cm, which vary by up to a factor of 2 between different scales, are *not* responsible for the observed spectral trends.

Previously, Anderson & Rudnick (1996) had claimed that the spectra of compact knots were similar to those of the underlying larger scale structure. However, their analysis was based on the *total* flux at the compact knots, which as seen here, is heavily contaminated by emission on a variety of larger scales. When the larger scale emission is filtered out, the remaining small-scale structures have flatter spectra, on average.

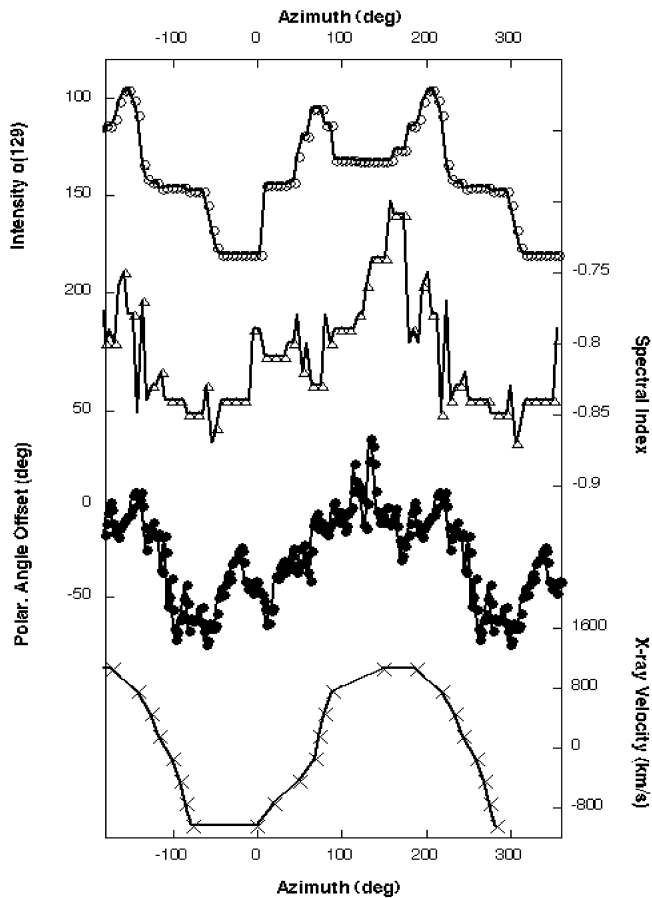


FIG. 27.—Four plots, as a function of azimuth, plotted over  $540^\circ$  to show the continuity, illustrating large-scale properties of Cas A. Open circles: intensity of  $\lambda 20$  cm  $o_{129}$  map. Triangles: Spectral index for  $o_{129}$  maps. Filled circles: Difference between magnetic field direction inferred from polarization at  $\lambda 6$  cm and the local azimuthal angle. Crosses: Line-of-sight velocity of X-ray-emitting plasma.

Note that there are still individual small-scale features, outside the bright ring and in the west, that have spectra as steep as the diffuse emission, as discussed below.

To look at the full distribution of spectral indices, we constructed spectral index maps by simple division of the respective pairs of filtered and open maps. The results are shown in Figure 26. In the first three filtered images, the steepest spectral indices are seen preferentially outside of the bright ring and in portions of the western higher brightness region interior to the bright ring. The range of spectral indices again covers the same small range, largely between  $-0.65$  and  $-0.9$ . This same range of spectral indices, as well as the location of the steepest spectra, was also found by Anderson & Rudnick (1996) in their spectral study of 304 compact components, which contain a total flux of only  $\approx 5$  Jy at  $\lambda 6$  cm.

The open maps showed a significant northwest-southeast asymmetry (Fig. 23). This would probably have been dismissed as a curiosity had not the same asymmetry been seen in other

properties. In Figure 27 we plot the intensity and spectral index from the open maps as a function of azimuth at a radius of  $\approx 100''$ , along with similar plots for the  $\lambda 6$  cm polarization angle (Anderson, Keohane, & Rudnick 1995) and the Doppler velocities of the X-ray Si-K lines from ASCA observations (Holt et al. 1994). The correspondence between these patterns is strong, and its significance is discussed below. This northwest-southeast asymmetry is seen clearly only in the diffuse emission and not in the filtered, small-scale components. The diffuse spectral indices show little, if any, gradient with radial distance.

### 5.1. The Structure and Relativistic Particle Populations of Cas A

As known for many years, Cas A's radio emission has a wide range of intrinsic scales, from  $0''.2$  (Arendt & Dickel 1987) to scales comparable to the remnant size. As shown for the first time here, the spectral indices of the small-scale and large-scale emission are different, in both average value and spatial distribution. The small-scale spectral behavior (Anderson & Rudnick 1996, hereafter AR96), which shows that the steep-spectrum components are predominantly found exterior to the bright ring, is not yet understood. Individual components are short lived, so they could plausibly be responsible for their own relativistic particle acceleration. However, their spectral indices are not tied to their respective dynamical states, which therefore argues against local regulation of the acceleration process. AR96 argued that the spectral indices were instead regulated by location, with the preexisting local particle populations illuminated in the presence of new high magnetic field features. That picture must now be reexamined because of the differences between the very diffuse and small-scale spectra.

Approximately 50% of the flux is in the diffuse component, but AR96 were not able to isolate it without the filtering techniques used here. The origins of the diffuse emission are unclear. They could represent the result of diffusion, from previous generations of small-scale shocks and other structures (see Atoyan et al. 2000), or simply electrons left behind as the high magnetic field regions dissipate. Alternatively, the diffuse population could arise from a truly diffuse particle acceleration process, separate from that in the high-field small-scale regions.

The diffuse emission shows a clear asymmetry between the northwest and southeast portions of the remnant. The simplest explanation for the X-ray asymmetry along the same axis is that we are viewing primarily the *back* of the incompletely illuminated shell in the northwest and primarily the *front* in the southeast. This is also consistent with the work of Lawrence et al. (1995), who show that the fast-moving knot population of ejecta show a very patchy distribution on a quasi-spherical shell, with large approaching rings of knots seen in the south and southeast and a large, mostly receding ring in the north and northwest. The same results are now visible in the X-ray Doppler maps of Willingale et al. (2002). The azimuthal variation in polarization angle, tracing this same pattern, is due

to rotation measure variations across the remnant (Kenney & Dent 1985). Such variations are expected since the thermal component seen in the X-rays and in the low-frequency radio absorption (Kassim et al. 1995) would produce a front-back path length/rotation measure gradient, again giving rise to a northwest-southeast asymmetry.

Currently, there is no model to explain why the spectra should be preferentially steeper in the rear (northwest) of the remnant. Reed et al. (1995) argue that the density is lower by about a factor of 5 in the rear hemisphere. However, the opposite spectral trend is seen for the steeper compact features in the west, where radio proper motions (Anderson & Rudnick 1993; Tuffs 1986) show significant deceleration and thus higher external densities. Resolution of these issues will depend on a more sophisticated understanding of the dominant epochs for relativistic particle evolution in the remnant's history and the origins of electron populations on different physical scales.

## 6. CONCLUSIONS

We have demonstrated the application of a simple filtering technique for separating emission on different angular scales in extragalactic and Galactic radio sources and evaluated its robustness and biases in a variety of circumstances. This multi-resolution method preserves the flux in each pixel, partitioning into the filtered and open maps. It can be used for quantitative measurements of brightness and spectra when appropriate care is taken. It avoids many of the problems of other methods that have been used for radio spectral measurements. Its advantages over other multiresolution visualization techniques are that it is trivial to implement and the artificial patchy structures that it produces can be easily recognized. Its primary disadvantage is that these same artificial structures clearly represent deviations from the actual sky brightness.

Using this technique, we find that extragalactic sources con-

tain small-scale structures in their lobes that have different spectra, usually flatter, than the surrounding diffuse emission. The underlying physical causes cannot be determined given the available information. For example, higher emissivity and flatter filamentary structures could plausibly result from high-field regions into which relativistic particles from the local medium have recently entered or low-field regions in which particles have traveled from the hot spot with lower losses than those in their surroundings. In the latter case, high-resolution observations at low frequencies would see the filaments as fainter areas, although this would be very difficult to detect.

Without knowing the history of the relativistic electron populations, i.e., their current and past magnetic field environments, it is impossible to assign a well-defined age to these filamentary structures on the basis of their spectral indices.

Applying this technique to the SNR Cas A, we find structures with a wide range of intrinsic scale sizes ( $<1''$  to  $>100''$ ) in the remnant. On the largest scales, the spectral indices show the same structure as the radio polarization and X-ray velocity images, presumably because of Cas A's front-back asymmetries and the fact that it is an incomplete shell. The spectral indices of the small-scale features are found to be flatter, in the mean, than those of large-scale features. These provide constraints for our still primitive understanding of relativistic particle acceleration in SNRs.

I gratefully acknowledge the use of data from M. Hardcastle and C. Carilli, combined with published observations from the Very Large Array and MERLIN. J. Dickey, T. W. Jones, B. Koralesky, K. Treichel, and A. Young provided useful discussions and comments on the manuscript. This work was supported, in part, at the University of Minnesota by the National Science Foundation under grants AST 96-16964, AST 96-19438, and AST 00-71167.

## REFERENCES

- Anderson, M. C., Keohane, J. W., & Rudnick, L. 1995, *ApJ*, 441, 300  
 Anderson, M. C., & Rudnick, L. 1993, *ApJ*, 408, 514  
 ———. 1995, *ApJ*, 441, 307  
 ———. 1996, *ApJ*, 456, 234 (AR96)  
 Arendt, R. G., & Dickel, J. R. 1987, *ApJ*, 315, 567  
 Atoyan, A. M., Aharonian, F. A., Tuffs, R. J., & Völk, H. J. 2000, *A&A*, 355, 211  
 Baars, J. W. M., Genzel, R., Pauliny-Toth, I. I. K., & Witzel, A. 1977, *A&A*, 61, 99  
 Carilli, C. L., Perley, R. A., Dreher, J. W., & Leahy, J. P. 1991, *ApJ*, 383, 554  
 Crawford, F., Gaensler, B. M., Kaspi, V. M., Manchester, R. N., Camilo, F., Lyne, A. G., & Pivovarov, M. J. 2001, *ApJ*, 554, 152  
 Hardcastle, M. J. 1999, *A&A*, 349, 381  
 Hardcastle, M. J., Alexander, P., Pooley, G. G., & Riley, J. M. 1997, *MNRAS*, 288, 859  
 Heiles, C., & Troland, T. H. 2002, preprint (<http://astron.berkeley.edu/heiles/papers/papers.html/zobs.ps>)  
 Holt, S. S., Gotthelf, E. V., Tsunemi, H., & Negoro, H. 1994, *PASJ*, 46, L151  
 Hook, I. M., Duffett-Smith, P. J., & Shakeshaft, J. R. 1992, *A&A*, 255, 285  
 Jaffe, W. J., & Perola, G. C. 1973, *A&A*, 26, 423  
 Jones, T. W., Ryu, D., & Engel, A. 1999, *ApJ*, 512, 105  
 Kassim, N. E., Perley, R. A., Swarakanath, K. S., & Erickson, W. C. 1995, *ApJ*, 455, L59  
 Katz-Stone, D. M., & Rudnick, L. 1994, *ApJ*, 426, 116  
 ———. 1997, *ApJ*, 488, 146  
 Katz-Stone, D. M., Rudnick, L., & Anderson, M. C. 1993, *ApJ*, 407, 549  
 Kenney, J. D., & Dent, W. A. 1985, *ApJ*, 298, 644  
 Lawrence, S. S., MacAlpine, G. M., Uomoto, A., Woodgate, B. E., Brown, L. W., Oliverson, R. J., Lowenthal, J. D., & Liu, C. 1995, *AJ*, 109, 2635  
 Lea, S. M., & Kellar, L. A. 1989, *AJ*, 97, 1238  
 Leahy, D., & Roger, R. S. 1991, *AJ*, 101, 1033

- Leahy, D., & Roger, R. S. 1998, *ApJ*, 505, 784
- Leahy, J. P., Black, A. R. S., Dennett-Thorpe, J., Hardcastle, M. J., Komissarov, S., Perley, R. A., Riley, J. M., & Scheuer, P. A. G. 1997, *MNRAS*, 291, 20
- Leahy, J. P., & Perley, R. A. 1991, *AJ*, 102, 537
- Ledden, J. E., Broderick, J. J., Condon, J. J., & Brown, R. L. 1980, *AJ*, 85, 780
- Mallat, S. G. 1989, *IEEE Trans. Pattern Anal. Machine Intell.*, 11, 674
- Reed, J., Hester, J., Fabian, A., & Winkler, F. 1995, *ApJ*, 440, 706
- Rudnick, L. 1999, preprint (astro-ph/9910202)
- Sanz, J. L., Argüeso, F., Cayón, L., Martínez-González, E., Barreiro, R. B., & Toffolatti, L. 1999, *MNRAS*, 309, 672
- Serra, J. 1982, in *Image Analysis and Mathematical Morphology* (New York: Academic), 34
- Starck, J. L., Murtagh, F., & Bijaoui, A. 1998, *Image Processing and Data Analysis: The Multiscale Approach* (Cambridge: Cambridge Univ. Press)
- Tregillis, I., Jones, T. W., & Ryu, D. 2001, *ApJ*, 557, 475
- Treichel, K., & Rudnick, L., Hardcastle, M., & Leahy, J. P. 2001, *ApJ*, 561, 691 (T01)
- Tuffs, R. J. 1986, *MNRAS*, 219, 13
- Willingale, R., Bleeker, J. A. M., van der Heyden, K. J., Kaastra, J. S., & Vink, J. 2002, *A&A*, 381, 1039
- Wright, M., Dickel, J., Koralesky, B., & Rudnick, L. 1999, *ApJ*, 518, 284